

1

2           **Single-dose immunisation with a multimerised SARS-CoV-2 receptor binding**  
3           **domain (RBD) induces an enhanced and protective response in mice**

4

5 Ralf Salzer<sup>1\*</sup>, Jordan J. Clark<sup>2\*</sup>, Marina Vaysburd<sup>1\*</sup>, Veronica T. Chang<sup>1\*</sup>, Anna Albecka<sup>1</sup>, Leo  
6 Kiss<sup>1</sup>, Parul Sharma<sup>2</sup>, Andres Gonzalez Llamazares<sup>1</sup>, Anja Kipar<sup>2, 3</sup>, Julian A. Hiscox<sup>2</sup>, Andrew  
7 Owen<sup>4</sup>, A. Radu Aricescu<sup>1</sup>, James P. Stewart<sup>2</sup>, Leo C. James<sup>1§</sup>, and Jan Löwe<sup>1§</sup>

8

9 1 - MRC Laboratory of Molecular Biology, Cambridge, UK

10 2 - Institute of Infection, Veterinary and Ecological Sciences, University of Liverpool, Liverpool,  
11 UK

12 3 – Laboratory for Animal Model Pathology, Institute of Veterinary Pathology, Vetsuisse  
13 Faculty, University of Zurich, Zurich, Switzerland

14 4 - Department of Pharmacology and Therapeutics, Centre of Excellence in Long-acting  
15 Therapeutics (CELT), University of Liverpool, UK.

16

17 \* Contributed equally to this work

18 § Corresponding authors: [lcj@mrc-lmb.cam.ac.uk](mailto:lcj@mrc-lmb.cam.ac.uk); [jyl@mrc-lmb.cam.ac.uk](mailto:jyl@mrc-lmb.cam.ac.uk)

19

20 Keywords: COVID-19; SARS-CoV-2; coronavirus; vaccine candidate; subunit vaccine; RBD; Dps

21 **ABSTRACT**

22 The COVID-19 pandemic, caused by the SARS-CoV-2 coronavirus, has triggered a worldwide  
23 health emergency. So far, several different types of vaccines have shown strong efficacy.  
24 However, both the emergence of new SARS-CoV-2 variants and the need to vaccinate a large  
25 fraction of the world's population necessitate the development of alternative vaccines,  
26 especially those that are simple and easy to store, transport and administer. Here, we showed  
27 that ferritin-like Dps protein from hyperthermophilic *Sulfolobus islandicus* can be covalently  
28 coupled with different SARS-CoV-2 antigens via the SpyCatcher system, to form extremely  
29 stable and defined multivalent dodecameric vaccine nanoparticles that remain intact even  
30 after lyophilisation. Immunisation experiments in mice demonstrated that the SARS-CoV-2  
31 receptor binding domain (RBD) coupled to Dps (RBD-S-Dps) shows particular promise as it  
32 elicited a higher antibody titre and an enhanced neutralising antibody response compared to  
33 the monomeric RBD. Furthermore, we showed that a single immunisation with the multivalent  
34 RBD-S-Dps completely protected hACE2-expressing mice from serious illness and led to  
35 efficient viral clearance from the lungs upon SARS-CoV-2 infection. Our data highlight that  
36 multimerised SARS-CoV-2 subunit vaccines are a highly efficacious modality, particularly when  
37 combined with an ultra-stable scaffold.

## 38 INTRODUCTION

39 On 11 March 2020 the World Health Organisation declared the COVID-19 outbreak, caused by  
40 the SARS-CoV-2 virus, a pandemic (Cucinotta and Vanelli, 2020). Since then, COVID-19 and the  
41 efforts to contain it have changed the lives of unprecedented numbers of people. For example,  
42 in April 2020 3.9 billion people were affected by lockdown measures aimed to cut or at least  
43 reduce the chain of transmission with widespread negative impacts on employment, education  
44 and other health issues. According to the Johns Hopkins University there have so far been  
45 151M confirmed COVID-19 cases globally (May 2021) and virtually every country has been  
46 affected. Officially, 3.2M people have died from SARS-CoV-2 infection (2021a, 2021b).

47 SARS-CoV-2 belongs to the family of *Coronaviridae*, which contain a positive-stranded RNA  
48 genome (Pal et al., 2020). The RNA is enveloped by a membrane that harbours four coat  
49 proteins (Fig. 1A). On the inside of the virus, the nucleocapsid protein (NP) is crucial for RNA  
50 packaging and viral release from host cells (Zeng et al., 2020). The Spike protein, which is  
51 embedded in the virus' membranous envelope, is essential for the interaction with human  
52 angiotensin-converting enzyme 2 (hACE2) (Ke et al., 2020). It is the interaction with hACE2 that  
53 is thought to initiate the process that leads to cell entry of viral RNA and infection (Shang et  
54 al., 2020). The Spike protein is translated as a single polypeptide that is proteolytically  
55 processed into its two subunits, S1 and S2. The Spike of SARS-CoV-2 is a trimer consisting of  
56 three S1-S2 heterodimers (Huang et al., 2020). For membrane fusion between the cell and the  
57 virus to occur, two cleavage events within the Spike complex are required (Ke et al., 2020). A  
58 protease cleavage site located between S1 and S2 is cleaved by the producer cell's proprotein  
59 convertase furin during virus assembly (Papa et al., 2021) (Fig. 1A). The second cleavage site is  
60 located in the S2 domain at position R797, and its hydrolysis by the target cell's surface  
61 protease TMPRSS2 triggers membrane fusion and cell entry (Papa et al., 2021).

62 The SARS-CoV-2 receptor-binding domain (RBD) is located within the S1 subunit of the Spike.  
63 It is the RBD that interacts directly with the host cell via the hACE2 receptor (Ke et al., 2020).  
64 It is therefore not surprising that antibodies directed against the RBD or overlap with the ACE2  
65 binding region are strongly neutralising, making the RBD a promising subunit vaccine candidate  
66 (Ke et al., 2020; Seydoux et al., 2020). The RBD is glycosylated and contains four disulphide

67 bridges that contribute to its stability, necessitating its expression in mammalian cells, as is  
68 also the case for the Spike.

69 To end the pandemic, vaccines are by far the most promising approach and vaccine  
70 developments, clinical trials, approvals and mass roll-outs are in progress. So far, until May  
71 2021, 89 COVID-19 vaccines have been tested in clinical trials. Of those, 36 are undergoing  
72 safety trials, 27 are in the phase of large-scale testing, 6 vaccines are authorised for limited  
73 use, and 8 vaccines are fully approved (2021a). All approved vaccines show good-to-excellent  
74 protection against severe illness and preliminary data have shown that virus transmission is  
75 significantly reduced in vaccinated individuals (Mahase, 2020; Thompson et al., 2021). Most of  
76 the approved vaccines and those in late-stage trials are mRNA-based, vector-based,  
77 inactivated viruses or DNA vaccines (Mahase, 2020). Vector- and RNA-based vaccines can often  
78 be rapidly developed because they deliver the immunogen coding sequence rather than the  
79 immunogen itself. Currently, only one vaccine candidate in late phase trials is a protein-based  
80 subunit vaccine, Novavax (Mahase, 2021). Some subunit vaccines are amenable to processes  
81 such as lyophilisation that remove the need for a complex storage and distribution cold-chain.  
82 As such, they provide substantial advantages over nucleic-acid based vaccines in the quest for  
83 complete and global vaccination. A second challenge facing global vaccination is the  
84 emergence of viral variants, some of which are more infectious and/or cause more severe  
85 illnesses, and reduce the efficacy of existing vaccines (Davies et al., 2021; Ferreira et al., 2021;  
86 Kupferschmidt, 2021; Zhang et al., 2021). Repeat vaccinations directed against these variants,  
87 but that use the same type of vaccine, could be problematic. This is because immunity is  
88 generated against the vaccine vector itself, neutralising it before it can deliver its immunogen  
89 cargo (Bottermann et al., 2018). It is anticipated that in future, several different types of  
90 vaccines will be required to cope with emerging variants of SARS-CoV-2.

91 Previous work has shown that protein-based subunit vaccines directed against SARS-CoV-2  
92 deliver high antibody responses in animal models (Tan et al., 2021; Wang et al., 2021).  
93 Furthermore, subunit antigens have the potential to deliver a cheaper, boostable and more  
94 robust alternative to nucleic-acid based vaccines (Dalvie et al., 2021; Gu et al., 2021; He et al.,  
95 2021; Joyce et al., 2021; Kalathiya et al., 2021; Koenig et al., 2021; Ma et al., 2020; Powell et  
96 al., 2021; Xiang et al., 2020). To explore the development of stable and efficient subunit vaccine  
97 candidates, we covalently linked SARS-CoV-2 proteins expressed in mammalian and bacterial



98 cells with bacterially-expressed Dps from the hyperthermophilic archaeon *Sulfolobus*  
99 *islandicus* (Gauss et al., 2006). Immunisation using SARS-CoV-2 RBD linked to Dps (RBD-S-Dps)  
100 proved to be highly effective in eliciting an immune response and to produce neutralising  
101 antibodies that inhibit cell entry *in vitro*. Furthermore, transgenic K18-hACE2 mice infected  
102 with SARS-CoV-2 were completely protected from serious illness following a single  
103 immunisation with RBD-S-Dps.

## 104 RESULTS

### 105 Three multimerised SARS-CoV-2 antigen complexes

106 We aimed to find a stable, convenient and non-bacterial display scaffold that would allow the  
107 display and multimerisation of a range of SARS-CoV-2 antigens (Fig. 1A). Multimerisation has  
108 been used for many years to increase the immunogenicity of different antigens through  
109 multivalency, and this approach has also been recently shown to work well with SARS-CoV-2  
110 antigens (Dalvie et al., 2021; Kalathiya et al., 2021; Powell et al., 2021; Wang et al., 2021).

111 For the purpose of stable multimerisation, we identified Dps (ORF SIL\_0492) from *Sulfolobus*  
112 *islandicus*. The source organism is an archaeon, which prefers pH ~3 and, as a  
113 hyperthermophile, has adapted to grow optimally at temperatures of around 80 °C. The  
114 intrinsic thermostability and environmental robustness of *S. islandicus* Dps make it an  
115 outstanding candidate for the development of a multimerisation scaffold. Dps, a member of  
116 the ferritin-like protein family, self-assembles into hollow, dodecameric spheres with 12  
117 subunits, which are roughly 10 nm across (Gauss et al., 2006). Most ferritins assemble larger  
118 spheres with 24 subunits. Also, in contrast to *bona fide* ferritin scaffolds, both the N- and the  
119 C-termini of Dps are accessible on the outside of the sphere.

120 We aimed to test whether Dps could efficiently display Spike, RBD and also NP antigens of  
121 SARS-CoV-2 (Fig. 1A). Spike and RBD cannot be expressed in folded form in *E. coli*, whereas NP  
122 as well as Dps express and fold well in *E. coli*. Expression of soluble and multimeric antigens  
123 genetically fused to Dps in mammalian cells (or *E. coli*) was unsuccessful, therefore we decided  
124 to employ the SpyCatcher/SpyTag system to attach Dps to different antigens. The  
125 SpyCatcher/SpyTag system forms isopeptide bonds between amino acid side chains of the  
126 catcher domain and the peptidic tag (Brune and Howarth, 2018; Zakeri et al., 2012). ΔN1-  
127 SpyCatcher (Bruun et al., 2018) was fused genetically to the N-terminus of Dps, separated by  
128 an eight amino acid long GS linker and a hexa-histidine tag added for purification purposes  
129 (SpyC-Dps, Fig. 1B & C). We chose N-terminal linkage to Dps, SpyC-Dps, rather than Dps-SpyC  
130 since the coupling reactions were more efficient, but we did not explore this in any detail. Both  
131 the N- and C- terminus of Dps are on the outside of the sphere and are accessible for covalent  
132 coupling. For the antigens, SpyTag2 sequences were fused either at the N- or C-termini, based  
133 on steric considerations (RBD-SpyT2, SpyT2-NP, Spike-SpyT2). Conjugation of stabilised and

134 trimeric Spike-SpyT2 to the dodecameric SpyC-Dps leads to polymerisation due to the  
135 multivalency of both partners. To overcome this problem, and to obtain a biochemically  
136 defined sample, we co-transfected HEK 293T Lenti-X cells with two different plasmids in a 3 to  
137 1 ratio, one expressing a SpyT2 version and one without SpyT2. This favoured the expression  
138 of Spike trimers in which only one of the monomers contains the SpyTag. Stabilised, trimeric  
139 and on average monovalent Spike-SpyT2 and also RBD-SpyT2 were purified from conditioned  
140 media of HEK 293S GnT1<sup>-/-</sup> (for Spike-SpyT2) or Expi 293 (for RBD-SpyT2) cell cultures. SpyC-  
141 Dps and SpyT2-NP were purified from the cytosol of *E. coli* cells transformed with the  
142 appropriate plasmids. All constructs possess histidine tags and were purified by immobilised  
143 metal affinity chromatography (IMAC) and at least one additional size exclusion step (SEC).  
144 Sequences of all proteins used can be found in Suppl. Table 1. Expression yields were excellent  
145 in all cases: SpyC-Dps yielded ~120 mg/L culture, RBD-SpyT2 ~40 mg/L culture, stabilised  
146 trimeric and monovalent Spike-SpyT2 ~13 mg/L culture and SpyT2-NP ~60 mg/L culture of pure  
147 proteins (Fig. 2A).

148 To achieve efficient coupling of scaffold and antigens, a molar excess of each of the three  
149 purified antigens (RBD-SpyT2, SpyT2-NP, Spike-SpyT2) was mixed with SpyC-Dps to facilitate  
150 covalent coupling. Subsequent removal of excess antigens was accomplished by SEC using a  
151 Superose 6 column (Fig. 2B). Coupling efficiency was analysed by SDS-PAGE, followed by  
152 Coomassie staining (Fig. 2C). When the coupled samples were mixed with denaturing SDS  
153 sample buffer without additional heating, we detected high molecular weight complexes that  
154 we suggest represent dodecameric assemblies caused by Dps that survive SDS treatment (“RT”  
155 lanes). Heating the samples to 99 °C led to the disappearing of the higher bands (“99” lanes),  
156 confirming both the (SDS-) stability and the purity of the coupled and multimerised protein  
157 samples. Note that there were no bands showing uncoupled SpyC-Dps in any of the three Ag-  
158 S-Dps samples, meaning that coupling used all 12 available Dps subunits.

159 Next, we analysed the integrity of the scaffold after the coupling reactions, as well as  
160 homogeneity by electron microscopy (Fig. 2D). For the scaffold alone, SpyC-Dps, we observed  
161 the expected small and well-dispersed ~10 nm Dps spheres. Similar homogeneity and  
162 monodispersity were observed for all three coupled Ag-S-Dps versions, RBD-S-Dps, NP-S-Dps  
163 and Spike-S-Dps. The Ag-S-Dps complexes were larger than the scaffold alone as the Dps  
164 spheres were densely surrounded by extra densities, indicating the success of the coupling and

165 the structural integrity of Ag-S-Dps complexes after the coupling reactions. We note that no  
166 aggregation was observed for Spike-S-Dps, indicating that the co-transfection approach  
167 produced mostly trimeric Spike proteins with only one SpyTag2 present. Taken together, we  
168 showed that the scaffold and the three antigens could be produced easily and at high yields  
169 and resulted in biochemically pure and defined Ag-S-Dps proteins that display 12 antigens on  
170 each Dps scaffold.

171 To determine whether the coupled Ag-S-Dps complexes were stable in blood plasma for  
172 immunisations, we mixed the RBD-S-Dps complex with human serum (clotted, not heat  
173 inactivated, at a 1:3 volume ratio). The RBD-S-Dps complex was remarkably stable, with 50%  
174 remaining intact after 37 h at 37 °C (Suppl. Fig. 1A & B). Given the stability of the Dps scaffold  
175 both in serum and when exposed to denaturing conditions (SDS-PAGE, “RT” lane) (Fig. 2C), we  
176 next investigated whether the coupled RBD-S-Dps sample would survive lyophilisation and  
177 subsequent re-solubilisation. A lyophilised, dry sample would facilitate prolonged storage even  
178 in the absence of refrigeration. We therefore freeze-dried RBD-S-Dps and after rehydration  
179 found no evidence of precipitation or significantly reduced protein concentration by SDS-PAGE  
180 (Suppl. Fig. 1C). There was also no disappearance of the SDS-stable high-molecular weight  
181 band, indicating Dps sphere integrity was maintained after re-hydration. Finally, electron  
182 microscopy analysis showed the rehydrated sample to be indistinguishable from the starting  
183 material with no evidence of disintegration or aggregation (Suppl. Fig. 1D).

#### 184 **Multimerisation by Dps greatly enhances immunogenicity, especially for RBD**

185 Having obtained the three multimerised antigen-Dps (Ag-S-Dps), we tested whether they  
186 induce a stronger immune response than their monomeric equivalents. We immunised mice  
187 with the following protocol: five male C57BL/6J mice per group were given 50 µg protein  
188 subcutaneously on days zero and 23, and 25 µg on day 64 (using CpG 1668 as an adjuvant) (Fig.  
189 3A). Blood samples were taken on days 13 (1<sup>st</sup> bleed), 34 (2<sup>nd</sup> bleed) and 74 (3<sup>rd</sup> bleed). After  
190 the 1<sup>st</sup> boost on day 34, antigen-specific antibodies were detected in the sera from the mice  
191 by ELISA (Fig. 3B). Substantially higher antibody titres were detected with multimerised Dps-  
192 fused RBD and NP. Multimerisation only improved Spike titres modestly, which may be  
193 expected given that Spike is already a trimer without Dps. After 74 days, and the second boost,  
194 the specific antibody titres were further increased. Spike induced the weakest response and

195 multimerisation had the smallest effect. In contrast, RBD-S-Dps and NP-S-Dps induced  
196 substantial increases in antibody titres compared to the non-multimerised versions. We also  
197 analysed sera for antibodies against the scaffold protein itself (SpyC-Dps). Sera from mice  
198 immunised with coupled Ag-S-Dps complexes showed measurable but low antibody titres  
199 against SpyC-Dps. Anti-SpyC-Dps responses remained low even after the second boost,  
200 suggesting that the scaffold itself is poorly immunogenic and that in the context of the fusions  
201 the antibody response is largely directed against the viral antigens displayed on the surface.  
202 Taken together the data show that multimerised Ag-S-Dps complexes produce substantial  
203 improvements in antibody titres over the uncoupled antigens. Overall, the strongest response  
204 was observed for RBD-S-Dps.

205 Next, we tested the neutralisation activity of antibodies produced by the mice immunised with  
206 RBD-S-Dps, RBD-SpyT2, Spike-S-Dps, and Spike-SpyT2. The mouse sera within each group were  
207 pooled at day 34 (2<sup>nd</sup> bleed) or 74 (3<sup>rd</sup> bleed) and analysed using a pseudovirus infection assay  
208 (note that NP-directed sera will not have an effect in this assay because pseudotyped viruses  
209 do not contain NP). In this assay, a lentiviral vector expressing GFP is pseudotyped with Spike  
210 protein from SARS-CoV-2 to obtain virions that display Spike in their envelope and infect cells  
211 in an ACE2-dependent manner. As seen in Figure 3C, the day 34 sera pool of the multimerised  
212 RBD-S-Dps group protected against pseudovirus infection up to a dilution of 1:400, whereas  
213 the monomeric RBD-SpyT2 only showed a protective effect at a 1:100 dilution, and even then  
214 only reduced infection by ~50%. Sera from mice immunised with multimeric Spike-S-Dps also  
215 protected against infection, whilst Spike-SpyT2 sera were unable to neutralise at any of the  
216 dilutions tested. The sera taken after 74 days had substantially increased neutralisation activity  
217 (Fig. 3D). The sera from RBD-S-Dps-immunised mice gave the strongest protection: even at a  
218 1:6400 dilution only ~10% infection could be detected. At this 1:6400 dilution, the monomeric  
219 RBD-SpyT2 and Spike-S-Dps sera gave very little neutralisation. While pseudoviruses are widely  
220 used to test the neutralisation activity of SARS-CoV-2 antisera, they are based on a lentiviral  
221 rather than coronavirus particle and do not recapitulate live virus replication. We therefore  
222 tested whether antibodies raised against multimeric RBD-S-Dps were capable of blocking a  
223 spreading infection of a primary clinical isolate of SARS-CoV-2. Viral replication was measured  
224 by RT-qPCR using probes against *NP* (gRNA) or *E* (sgRNA). RBD-S-Dps antisera from five  
225 different animals all potently inhibited SARS-CoV-2 (Suppl. Fig. 2A & B). In contrast, the potency

226 of antisera raised against RBD-SpyT2 varied considerably between mice. We conclude that  
227 immunisation with RBD-S-Dps not only produces the highest titre antibodies (Fig. 3B), but also  
228 the most neutralising (Fig. 3C & D) and with reliable potency against live virus (Suppl. Fig. 2A &  
229 B).

### 230 **Single-shot immunisation with multimerised RBD-S-Dps protects mice against SARS-CoV-2** 231 **infection**

232 Encouraged by these results, we wanted to know if antigen display on our Dps scaffold would  
233 induce a sufficiently strong antibody response to protect animals from SARS-CoV-2 infection.  
234 We selected our most potent immunogen, RBD-S-Dps, and used it to immunise mice transgenic  
235 for human ACE2 (K18-hACE2) (Zheng et al., 2021). As a single dose vaccination regime offers  
236 many downstream logistical and practical benefits, we opted to immunise only once and then  
237 challenge with SARS-CoV-2 on day 28 (Fig. 4A). We immunised subcutaneously six K18-hACE2  
238 mice with RBD-S-Dps, six with RBD-SpyT2 and six with PBS (always three female and three male  
239 mice), each with 25 µg of the immunogens (except PBS control), plus CpG adjuvant. The anti-  
240 Spike antibody response following immunisation was measured by ELISA on days 13 and 24  
241 (before challenge) and on day 35, (seven days post-challenge). A strong anti-Spike antibody  
242 titre was detected in RBD-S-Dps-immunised mice, but almost none for either RBD-SpyT2 or  
243 PBS (Fig. 4D). Antibody titres remained high for RBD-S-Dps at days 24 and 35.

244 On day 28, animals were challenged with  $10^4$  PFU SARS-CoV-2. Mice in the PBS control and  
245 RBD-SpyT2-immunised groups began to show clinical signs of illness and a decline in body  
246 weight from day four post-infection (Fig. 4B), consistent with previous reports of infection in  
247 naïve animals (Zheng et al., 2021). In contrast, mice immunised with multimerised RBD-S-Dps  
248 maintained body weight until the day seven end point. There was a statistically significant  
249 difference in weights between the RBD-S-Dps-immunised and PBS control groups from day  
250 four, and between RBD-S-Dps- and RBD-SpyT2-immunised mice from day five (Fig. 4C). There  
251 was no significant difference in weight loss between the RBD-SpyT2-immunised mice and PBS  
252 controls at any time point, suggesting that, unlike RBD-S-Dps, non-multimerised RBD does not  
253 provide protection after only a single vaccination. All animals were culled on day seven post-  
254 infection and tissues collected for analysis. As mentioned, there were no significant changes in  
255 anti-Spike antibody levels pre- versus post-challenge, indicating that mostly antibodies raised

256 during the immunisation contributed to the immune response during the infection (Fig. 4D).  
257 SARS-CoV-2 infection of the lung was quantified by plaque assay and genomic and subgenomic  
258 qPCR, using probes against the viral genes NP and E, respectively. There were significantly  
259 lower levels of infectious virus in the lungs of mice immunised with RBD-S-Dps, compared to  
260 either RBD-SpyT2 immunised or PBS control groups (Fig. 4E). A broadly similar pattern was  
261 observed when quantifying virus by either genomic or subgenomic qPCR (Fig. 4F & G).  
262 However, we noted a marked difference in the amounts detected between male vs female  
263 mice. Female RBD-S-Dps-immunised mice had significantly fewer genomic and subgenomic  
264 transcripts, compared to mice from other groups and their male equivalents (Fig. 4F & G and  
265 Suppl. Fig. 3A & B). We attempted to correlate this with differences in antibody titres, but while  
266 there was a trend towards lower titres in male mice, particularly just before and just after the  
267 challenge, this was not significant (Suppl. Fig. 3C). A larger group size would be needed to  
268 confirm this result. Despite these sex-dependent differences in the qPCR data, the near-  
269 absence of infectious virus in both male and female RBD-S-Dps immunised mice, as measured  
270 by plaque assay (Suppl. Fig. 3D), suggests they were both highly protected. Finally, we  
271 examined the lungs of mice from the different groups for histopathological changes and for  
272 viral antigen expression using an anti-NP antibody to reveal sites of replication (Fig. 4H, Suppl.  
273 Fig. 4) and immune cell infiltration (Suppl. Fig. 5). A detailed description is provided in the  
274 Supplementary Results. In summary, lungs from RBD-SpyT2-immunised mice or PBS control  
275 mice showed substantial and wide-spread NP expression mainly in pneumocytes (Fig. 4H &  
276 Suppl. Fig. 4), indicative of viral replication throughout the lobe and consistent with the high  
277 virus levels measured in these animals (Fig. 4E-G). There was also evidence of pneumocyte  
278 degeneration and syncytial cell formation, as has been reported in COVID-19 cases post-  
279 mortem (Bussani et al., 2020). Multifocal leukocyte infiltration was observed, particularly in  
280 PBS-control animals, dominated by macrophages, followed by T-cells (mainly CD4+ and lesser  
281 CD8+ cells), B cells and neutrophils (Suppl. Fig. 4 & 5). This is reminiscent of the  
282 hyperinflammation in post-mortem reports of lethal COVID-19 associated with  
283 immunopathology (Schurink et al., 2020). In contrast, the lungs of mice protected by  
284 multimerised RBD-S-Dps were either almost or entirely clear of NP expression (Suppl. Fig. 4)  
285 and pathological changes (female mice), or showed only mild changes consistent with those  
286 observed in the PBS-control animals (Suppl. Fig. 5), and markedly reduced NP expression.  
287 Taken together, these data indicate that immunisation with RBD-S-Dps is highly protective

288 against SARS-CoV-2 in hACE2-expressing mice, even after a single dose, whilst monomeric RBD-  
289 SpyT2 is not.



## 290 DISCUSSION

291 Here we have shown that the ferritin-like protein Dps from the hyperthermophile *S. islandicus*  
292 possesses exceptional qualities as a SARS-CoV-2 subunit vaccine scaffold. We combined Dps  
293 with the SpyCatcher/SpyTag system in order to create a “plug-and-play” system that allows  
294 the rapid and facile synthesis of highly stable multimeric subunit vaccines. Mixing the  
295 SpyCatcher-Dps protein with any compatible SpyTag antigen leads to the assembly of highly  
296 monodisperse nanoparticles displaying exactly 12 antigens. Using this approach, we have  
297 produced subunit vaccines based on Spike, RBD or NP from SARS-CoV-2 and tested them in  
298 immunisation and viral challenge experiments. In each case, the Dps-displayed antigens out-  
299 performed their non-multimerised equivalents and induced a more rapid and potent antibody  
300 response.

301 Subunit vaccines offer distinct advantages in cost, simplicity, production capacity, storage,  
302 transport and administration over nucleic-acid based vaccines (Pollet et al., 2021). Principle  
303 amongst these considerations is stability, with currently used vaccines such as those produced  
304 by Pfizer–BioNTech, Moderna and Oxford-AstraZeneca requiring a -80°C or -20°C cold-chain.  
305 In countries without a highly developed logistical and medical infrastructure this represents a  
306 significant impediment to vaccination. Whilst subunit vaccine development currently lags  
307 behind nucleic-acid based equivalents, there is good evidence that such vaccines are  
308 nevertheless effective at inducing a protective response. SARS-CoV-2 RBD by itself (Yang et al.,  
309 2020) or in simple fusions such as to IgG Fc (Liu et al., 2020) have been shown to elicit SARS-  
310 CoV-2-neutralising antibodies. Antigen multimerisation increases neutralising titres, for  
311 instance when using ferritin as a scaffold (He et al., 2021; Powell et al., 2021). More complex  
312 scaffolds have also been used, for instance virus-like icosahedral particles that display 60  
313 antigen copies (e.g. I3-01) (Hsia et al., 2016). When fused directly to viral antigens (Walls et al.,  
314 2020), or using the SpyCatcher/SpyTag system (Cohen et al., 2021; Tan et al., 2021) the I3-01  
315 scaffold has been shown to induce a neutralising antibody response. Our scaffold differs from  
316 those previously used to deliver SARS-CoV-2 immunogens in several important aspects. First,  
317 because we have used a thermostable protein it is intrinsically more stable, providing potential  
318 benefits to vaccine transport and storage and also to immunogen stability *in vivo*. Second, it is  
319 smaller than other scaffolds (< 10 nm vs > 10 nm for ferritin or 25 nm for the I3-01  
320 nanoparticle), making it an easier cargo for cellular uptake. Third, it displays fewer copies than

321 ferritin or I3-01 (12 vs 24 or 60, respectively), allowing the selection of higher-affinity B cells  
322 and avoiding the activation of off-target (and possibly cross-reactive) B cell competitors (Kato  
323 et al., 2020). Fourth, in contrast to *bona fide* ferritin scaffolds, the N- and the C-termini of Dps  
324 are both accessible on the outside of the sphere. This allows, at least in principle, for the  
325 conjugation of two discrete antigens onto a single scaffold, for example both SARS-CoV-2  
326 Spike/RBD and NP to be displayed simultaneously.

327 Importantly, we have provided here data demonstrating the benefit of antigen  
328 multimerisation in inducing not just neutralising antibodies but an immune response capable  
329 of providing *in vivo* protection. In our SARS-CoV-2 challenge experiments, we found that RBD  
330 alone failed to protect mice, which displayed continued weight-loss and high viral loads in the  
331 lungs. In contrast, our Dps-based vaccine displaying RBD completely protected mice from  
332 SARS-CoV-2-associated pneumonia and disease after only a single immunisation. We noted  
333 however a difference in Dps-RBD induced protection between male and female mice, with the  
334 latter having lower viral loads and hardly any pulmonary changes. Trial data for both mRNA  
335 and vector-based vaccines has not been disaggregated by sex but data on SARS-CoV-2 infection  
336 show that men are more at risk of severe adverse conditions, hospitalisation and death (Klein  
337 et al., 2020; Scully et al., 2020). Our results support the consideration of sex as a variable in  
338 vaccine trials (Bischof et al., 2020).

339 Further research is needed to develop the Dps-scaffold into a *bona fide* vaccine for SARS-CoV-  
340 2 and other viruses. Replicating the robust neutralising antibody response and high-level of  
341 protection achieved in mice from a single dose in humans will be crucial. Moreover, whilst  
342 most studies of subunit vaccines have focused on antibodies, long-lasting protection is likely  
343 to be dependent upon stimulating CD4+ and CD8+ T cell immunity (Sauer and Harris, 2020; Zuo  
344 et al., 2021). Data from current vaccine trials and roll-outs has yet to be fully analysed but a  
345 correctly balanced T cell response appears associated with recovery from acute infection and  
346 the avoidance of hospitalisation and severe virus-induced immunopathology (Chen and John  
347 Wherry, 2020). Fortunately, the analysis of T cell epitopes from SARS-CoV-2 convalescents  
348 (Nelde et al., 2021) provides a basis for engineering subunit vaccines specifically to engage  
349 both B and T cells. In this context, the ability of our Dps-scaffold to display antigens at both  
350 termini may prove particularly beneficial. In addition to ensuring a well-balanced immune  
351 response in humans, a more thorough investigation into the long-term stability, storage and

352 reconstitution of lyophilised material is required to demonstrate that a Dps-based vaccine is  
353 suitable for use in regions with limited infrastructure. Future work notwithstanding, our data  
354 add to a body of evidence that subunit-based vaccines represent a viable choice as a vaccine  
355 modality for SARS-CoV-2. Whilst other vaccine formats are significantly more advanced,  
356 subunit approaches such as Dps offer distinct advantages in simplicity of production, requiring  
357 no proprietary technology, robustness of material and potency of protection.

## 358 MATERIAL & METHODS

### 359 Cloning, expression and purification of the protein components

360 **SpyC-Dps:** a hexa-histidine tag was fused to  $\Delta$ N1-SpyCatcher, which was subsequently linked  
361 to the Dps from *Sulfolobus islandicus* (ORF SIL\_0492, GenBank AGJ61963.1), separated by a  
362 GSEGSSGG-linker (Suppl. Table 1, SpyC-Dps). The sequence was codon optimised for the  
363 expression in *E. coli* and the gene was cloned into the pOPINS vector by Gibson assembly. The  
364 plasmid encoding for SpyC-Dps was transformed into C43(DE3) *E. coli*. Cells were grown at 37  
365 °C in 2xYT medium to an OD<sub>600</sub> of 0.8. Protein production was induced with 1 mM IPTG for 6 h.  
366 Cells were harvested at 4500 x g for 25 min at room temperature (RT). Cells were shock-frozen  
367 in liquid nitrogen (LN2) and stored at -80 °C. Cells producing SpyC-Dps were re-suspended in  
368 T-buffer1 (30 mM Tris, 250 mM NaCl, pH 8.0) with one tablet of Complete Protease Inhibitors  
369 (Roche) per 10 g cells wet weight. Cell disruption was carried out using sonication for 7.5 min  
370 “on” time, using a 50 % duty cycle. Cell debris were removed by centrifugation at 20,000 x g  
371 for 30 min at RT. The supernatant was loaded onto a HisTrap FF affinity chromatography  
372 column (Cytiva). Washing was carried out for 17 column volumes (CV) with T-buffer1 plus 110  
373 mM imidazole. The protein was eluted with T-buffer1 containing 400 mM imidazole. Purity of  
374 fractions was examined by SDS-PAGE and the purest fraction were pooled and concentrated  
375 using a Vivaspin Turbo centrifugal concentrator (100,000 MWCO, Sartorius). Concentrated  
376 sample was loaded onto a size-exclusion column (SEC, Sephacryl S-400, Cytiva), with PBS as  
377 the running buffer. Purity was examined by SDS-PAGE and the sample was frozen in LN2 and  
378 stored at -80 °C.

379 **SpyT2-NP:** the nucleocapsid protein (amino acids 48 - 364; GenBank: MN908947; NP) was  
380 cloned into the vector pOP-TH and N-terminally equipped with a hexa-histidine tag (Pickering  
381 et al., 2020). A SpyTag2 sequence separated by GS-rich linkers was inserted between the hexa-  
382 histidine tag and NP (Fig. 1 & Suppl. Table 1, SpyT2-NP). The vector encoding for SpyT2-NP was  
383 transformed into *E. coli* C41(DE3) cells. For protein expression, cells were grown at 37 °C in  
384 2xYT medium to an OD<sub>600</sub> of 0.7. Protein production was induced with 1 mM IPTG for 6 h. Cells  
385 were harvested at 4500 x g for 25 min at 4 °C. Cells were frozen in LN2 and stored at -80 °C.  
386 SpyT2-NP-producing cells were re-suspended in T-buffer2 (50 mM Tris, 1 M NaCl, 10 mM  
387 imidazole, 2 mM DTT, pH 8.0) with Complete Protease Inhibitor added (1 tablet per 10 g cells

388 wet weight). Cells were lysed by sonication (3 mins total “on” time, duty cycle 50 %).  
389 Precipitated proteins and cell debris were removed by centrifugation (40,000 x g, 1 h, 4 °C).  
390 The supernatant was loaded onto a HisTrap FF affinity chromatography column and washed  
391 with 20 CV T-Buffer3 (50 mM Tris, 300 mM NaCl, 1 mM DTT, pH 8.0) containing 20 mM  
392 imidazole. Elution was carried out in T-buffer3 containing 400 mM imidazole. Elution fractions  
393 containing NP were loaded onto 20 ml HiTrap Heparin HP column equilibrated in T-buffer4 (50  
394 Tris, 1 mM DTT, pH 8.0). The column was washed with 3 CV T-buffer4. Elution was carried out  
395 with a linear gradient of 0 - 2 M NaCl. Elution fractions containing SpyT2-NP were examined by  
396 SDS-PAGE and pooled, and concentrated using a Vivaspin Turbo concentrator with a 10,000  
397 MWCO (Sartorius). Concentrated sample was loaded onto a SEC column (Sephacryl S-200)  
398 (Cytiva) in PBS + 250 mM additional NaCl. Purity was checked by SDS-PAGE and samples were  
399 frozen in LN2 and stored at -80 °C.

400 **Spike-SpyT2 and Spike:** to express the ectodomain of the stabilised prefusion Spike protein  
401 trimer (Wrapp et al., 2020) with only one subunit carrying the SpyTag2 tag, two constructs –  
402 one with and one without a SpyTag2 - were made. First, a gene encoding residues 16-1208 of  
403 SARS-CoV-2 Spike protein (GenBank: MN908947) with proline substitutions at residues 986  
404 and 987, a GSAS substitution at the furin cleavage site (residue 682-685), a C-terminal T4  
405 fibritin trimerisation motif, a GGSGGS linker, an HRV3C protease cleavage site, a GGS linker  
406 and an AviTag, was synthesised and cloned into the lentiviral expression vector pHR-SFFV  
407 (Chang et al., 2015, 2016; Elegheert et al., 2018) downstream of the sequence encoding the  
408 chicken RPTP $\sigma$  secretion signal peptide (cRPTP $\sigma$ SP) (Aricescu et al., 2006). Then, either a GGS  
409 linker and a hexa-histidine tag, or a GGS linker, an octa-histidine tag, a GGSGSGGS linker and  
410 a SpyTag2 were inserted after the AviTag sequence to form two Spike constructs, with and  
411 without a SpyTag2 (Suppl. Table 1, Spike-SpyT2 and Spike, respectively). For protein expression  
412 and purification, please see the next paragraph.

413 **RBD-SpyT2:** a gene encoding residue 332-529 of SARS-CoV-2 Spike protein (constituting the  
414 receptor binding domain, RBD) was synthesised and cloned downstream of cRPTP $\sigma$  of the pHR-  
415 SFFV vector and a GGSGGS linker, an AviTag, a GGS linker, an octa-histidine tag, a GGSGSGGS  
416 linker and a SpyTag2 were inserted at the 3' end of the gene (Suppl. Table 1, RBD-SpyT2). The  
417 vectors for Spike-SpyT2, Spike and RBD-SpyT2 were used for protein production in the  
418 mammalian lentiviral expression system (Chang et al., 2015, 2016; Elegheert et al., 2018). The

419 DNA of the constructs was mixed with the lentiviral envelope and packaging vectors pMD2-G  
420 and psPAX2c (Addgene) and polyethylenimine (PEI, Sigma) to transiently transfect HEK 293T  
421 Lenti-X cells (Takara/Clontech) to make lentiviral particles. To make Spike trimer protein with  
422 only one subunit carrying a SpyTag2, the DNAs of constructs Spike and Spike-SpyT2 were used  
423 at a molar ratio 3:1. The virus particles produced were used to infect HEK 293S GnT1<sup>-/-</sup> cells  
424 (for Spike-SpyT2) or Expi 293 cells (for RBD-SpyT2). The infected cells were then expanded to  
425 obtain 3 L cultures and conditioned media were harvested and sterile filtered (0.22 µm). The  
426 supernatant was concentrated and the buffer exchanged to 25 mM Tris pH 8.0, 300 mM NaCl  
427 using an Äkta flux tangential flow system (Cytiva). The conditioned supernatant was then  
428 loaded onto a HisTrap column (Cytiva) and washed and eluted with 50 mM and 250 mM  
429 imidazole in the same buffer, respectively. Eluted fractions were checked by SDS-PAGE, pooled  
430 and further purified in PBS buffer by SEC on Superdex 200 for RBD and Superose 6 for trimeric  
431 Spike protein (both Cytiva). Peak fractions were checked by SDS-PAGE again and frozen in LN2  
432 and stored at -80 °C.

#### 433 **Coupling and purification of multimerised complexes**

434 For the preparations of Ag-S-Dps complexes, comprising RBD-S-Dps, NP-S-Dps and Spike-S-Dps  
435 the antigens: RBD-SpyT2, SpyT2-NP and Spike/Spike-SpyT2, and the scaffold protein SpyC-Dps  
436 were diluted in PBS buffer + 250 mM NaCl to 0.2 to 1 mg/mL and mixed. To achieve full  
437 occupancy of SpyC-Dps with the antigens, the molar ratio for SpyC-Dps to RBD-SpyT2 was 1:1.3,  
438 for SpyT2-NP 1:2 and for trimeric Spike/Spike-SpyT2 1:2.5. Reactions were left for ~5 min at RT  
439 and covalent coupling between SpyCather2 and SpyTag2 was checked by SDS-PAGE.  
440 Subsequently, samples were concentrated using Vivaspin Turbo concentrators (100,000  
441 MWCO). Antigen-decorated SpyC-Dps complexes were separated from the excess antigens by  
442 SEC in PBS + 250 mM NaCl on a Superose 6 Increase column (Cytiva). Fractions were checked  
443 again for purity by SDS-PAGE, frozen in LN2 and stored at -80 °C.

#### 444 **Negative-stain electron microscopy**

445 Proteins were diluted in PBS to concentrations of ~0.012 mg/mL. 3 µL of the solution were  
446 applied to a glow-discharged carbon-coated grid and immediately blotted. For the staining, 10  
447 µL of 2% (w/v) uranyl formate were applied and removed immediately by blotting the grid with

448 filter paper. Images were collected on a FEI Tecnai Spirit 120 kV electron microscope, equipped  
449 with a CCD detector.

#### 450 ***In vitro* human plasma stability assay**

451 The *in vitro* stability of RBD-S-Dps was studied in clotted human plasma (MD Biomedicals, cat.  
452 #2930149). Stocks of the RBD-S-Dps samples (751.7 kDa per dodecameric complex) were  
453 diluted in PBS to a final concentration of ~0.8  $\mu$ M and subsequently mixed with pre-warmed  
454 human plasma in a 1:3 (protein:plasma, v/v) ratio. The mixtures were incubated at 37 °C for  
455 seven days. Samples were taken after 0, 1, 24, 48, 72, 96, 120 and 168 h, and immediately  
456 mixed with denaturing gel-loading buffer, followed by 30 min incubation at 99 °C. Inactivated  
457 samples were stored at -20 °C before the samples were diluted 1:10 with 1x SDS sample buffer  
458 and 5  $\mu$ L per sample were analysed by SDS-PAGE and Western blotting. The Ag-S-Dps  
459 complexes were detected using the HisProbe-HRP (Thermo Fisher Scientific, TFS) and human  
460 transferrin was used as a loading control and detected using transferrin antibodies from  
461 chicken and chicken-HRP conjugated antibodies (Thermo Fisher Scientific, TFS, cat. #PA1-9525  
462 and cat. # 31401).

#### 463 **Lyophilisation of samples**

464 An aliquot of RBD-S-Dps of 120  $\mu$ L (at a protein concentration of 1.4 mg/mL, in PBS buffer plus  
465 additional 250 mM NaCl) was divided into a 40  $\mu$ L control and a second aliquot of 80  $\mu$ L. The  
466 80  $\mu$ L aliquot was lyophilised for 4 h at 30 °C with the aid of a vacuum concentrator (Eppendorf  
467 Concentrator 5301) attached to a refrigerated condensation trap (Savant). After lyophilisation  
468 to complete dryness, the sample was resuspended in 80  $\mu$ L Milli-Q water. The sample was not  
469 centrifuged or processed in any other way after rehydration. EM grids were prepared by  
470 staining 1:20 and 1:100 dilutions (in PBS plus 250 mM NaCl) of lyophilised and resuspended  
471 sample with 2 % uranyl formate solution on carbon-coated CF400-CU-UL grids (Electron  
472 Microscopy Sciences) as described earlier. Imaging was also performed as described earlier. 10  
473  $\mu$ L of lyophilised and rehydrated sample and the untreated control were compared by SDS-  
474 PAGE followed by Coomassie staining.

#### 475 **Mouse immunisation (Fig. 3)**

476 Six weeks-old C57BL/6J mice (Jackson) were used in immunisation experiments, which were  
477 conducted in accordance with the E7 moderate severity limit protocol and the UK Home Office  
478 Animals (Scientific Procedures) Act (ASPA, 1986), and approved by the UKRI Animal Welfare  
479 and Ethical Review Body. Mice were initially (prime) immunised subcutaneously with 50 µg of  
480 the antigens in PBS, mixed with 10 µg CpG ODN 1668 adjuvant (InvivoGen). The following  
481 antigens were used: RBD-S-DPS, RBD-SpyT2; NP-S-DPS, SpyT2-NP; Spike-S-DPS, Spike/Spike-  
482 SpyT2 and SpyC-Dps. Mice were subcutaneously boosted with 50 µg antigens at day 23 and  
483 with 25 µg antigens at day 64. Tail bleeds for ELISA analyses were collected on days 13 and 34.

#### 484 **Preparation of SARS-CoV-2 Spike-pseudotyped HIV-1 virions**

485 Replication deficient SARS-CoV-2 pseudotyped HIV-1 virions were prepared as described  
486 previously (Morecroft and Thomas, 1988). Briefly, virions were produced in HEK 293T cells by  
487 transfection with 1 µg of the plasmid encoding SARS CoV-2 Spike protein (pCAGGS-SpikeΔc19),  
488 1 µg pCRV GagPol and 1.5 µg GFP-encoding plasmid (CSGW). Viral supernatants were filtered  
489 through a 0.45 µm syringe filter at 48 h and 72 h post-transfection and pelleted for 2 h at  
490 28,000 x g. Pelleted virions were drained and then resuspended in DMEM (Gibco).

#### 491 **Spike-pseudotyped neutralisation assays with mouse sera**

492 HEK 293T-hACE2-TMPRSS2 cells were described previously (Papa et al., 2021). Cells were  
493 plated into 96-well plates at a density of  $0.75 \times 10^3$  cells per well and allowed to attach  
494 overnight. 20 µL pseudovirus-containing supernatant was mixed with 2 µL dilutions of heat-  
495 inactivated mouse sera and incubated for 40 min at RT. 10 µL of this mixture was added to  
496 cells. 72 h later, cell entry was detected through the expression of GFP by visualisation on an  
497 Incucyte S3 live cell imaging system (Sartorius). The percent of cell entry was quantified as GFP  
498 positive areas of cells over the total area covered by cells. Entry inhibition by the sera was  
499 calculated as percent virus infection relative to virus only control.

#### 500 **ELISA assays**

501 96-well plates (Nunc) were coated overnight with 5 µg/mL of the indicated antigens. Plates  
502 were blocked with MPBST: 2 % (v/v) milk in PBS, 0.05 % Tween 20. Polyclonal sera from  
503 individual mice (challenge experiment) or mouse sera pooled within the same group (mouse



504 immunisation) were diluted as indicated with MPBST and incubated for 45 min on antigen-  
505 coated plates. Plates were washed with MPBST and bound antibodies were detected with goat  
506 anti-mouse IgG-HRP (Jackson ImmunoResearch, #115-035-071).

#### 507 **Cell culture and virus**

508 UK strain of SARS-CoV-2 (hCoV-2/human/Liverpool/REMRQ0001/2020; PANGO lineage B), was  
509 used and grown to P4 in Vero E6 cells (Patterson et al., 2020). The intracellular viral genome  
510 sequence and the titre of virus in the stock was determined by direct RNA sequencing  
511 (Genbank: MW041156). The virus stock did not contain a deletion of the furin cleavage that  
512 has been described previously during passage (Davidson et al., 2020).

#### 513 **Mouse SARS-CoV-2 challenge experiment**

514 Animal work was approved by the local University of Liverpool Animal Welfare and Ethical  
515 Review Body and performed under UK Home Office Project Licence PP4715265. Mice carrying  
516 the human ACE2 gene under the control of the keratin 18 promoter (K18-hACE2; formally  
517 B6.Cg-Tg(K18-ACE2)2PrImn/J) were purchased from Jackson Laboratories. Mice were  
518 maintained under SPF barrier conditions in individually ventilated cages. Animals were  
519 randomly assigned into multiple cohorts and given 25 µg antigen (RBD-S-DPS or RBD-SpyT2) &  
520 10 µg CpG or PBS via subcutaneous injection. On day 28 post-immunisation, mice were  
521 anaesthetised lightly with isoflurane and inoculated intranasally with 50 µL containing 10<sup>4</sup> PFU  
522 SARS-CoV-2 in PBS. They were culled on day 35 post-immunisation by an overdose of  
523 pentobarbitone. Tissues were removed immediately for downstream processing.

#### 524 **RNA extraction and DNase treatment**

525 The upper lobes of the right lung were dissected and homogenised in 1 mL of TRIzol reagent  
526 (TFS) using a Bead Ruptor 24 (Omni International) at 2 meters per second for 30 s. The  
527 homogenates were clarified by centrifugation at 12,000 x g for 5 min before full RNA extraction  
528 was carried out according to manufacturer's instructions. RNA was quantified and quality  
529 assessed using a Nanodrop (TFS) before a total of 1 µg was DNase treated using the TURBO  
530 DNA-free kit (TFS) as per manufacturer's instructions.

#### 531 **qRT-PCR for viral load**

532 Viral loads were quantified using the GoTaq® Probe 1-Step RT-qPCR System (Promega). For  
533 quantification of SARS-CoV-2 the nCoV\_N1 primer/probe mix from the SARS-CoV-2 (2019-  
534 nCoV) CDC qPCR Probe Assay (IDT) were utilised while the standard curve was generated via  
535 10-fold serial dilution of the 2019-nCoV\_N\_Positive Control (IDT) from 10<sup>6</sup> to 0.1  
536 copies/reaction. The E sgRNA primers and probe have been previously described (Wölfel et al.,  
537 2020) and were utilised at 400 nM and 200 nM respectively. Murine 18S primers and probe  
538 sequences were utilised at 400 nM and 200 nM respectively. The IAV primers and probe  
539 sequences were published as part of the CDC IAV detection kit (20403211). The IAV reverse  
540 genetics plasmid encoding the NS segment was diluted 10-fold from 10<sup>6</sup> to 0.1 copies/reaction  
541 to serve as a standard curve. The thermal cycling conditions for all qRT-PCR reactions were as  
542 follows: 1 cycle of 45 °C for 15 min and 1 cycle of 95 °C followed by 40 cycles of 95 °C for 15 s  
543 and 60 °C for 1 min The 18S standard was generated by the amplification of a fragment of the  
544 murine 18S cDNA using the primers F: ACCTGGTTGATCCTGCCAGGTAGC and R:  
545 GCATGCCAGAGTCTCGTTCG. Similarly, the E sgRNA standard was generated by PCR using the  
546 qPCR primers. cDNA was generated using the SuperScript IV reverse transcriptase kit (TFS) and  
547 PCR carried out using Q5 High-Fidelity 2X Master Mix (New England Biolabs) as per  
548 manufacturer's instructions. Both PCR products were purified using the QIAquick PCR  
549 Purification Kit (Qiagen) and serially diluted 10-fold from 10<sup>10</sup> to 10<sup>4</sup> copies/reaction to form  
550 the standard curve.

## 551 **Histology and immunohistology**

552 The left lung lobes were fixed in formal saline for 24 h and routinely paraffin wax embedded.  
553 Consecutive sections (3-5 µm) were either stained with haematoxylin and eosin (HE) or used  
554 for immunohistology (IH). IH was performed to detect SARS-CoV-2 antigen and leukocyte  
555 subtypes, i.e. T cells (CD3+, CD4+, CD8+), B cells (CD45R/B220+) and macrophages (Iba1+),  
556 using the horseradish peroxidase (HRP) method and the following primary antibodies: rabbit  
557 anti-SARS-CoV NP (Rockland, 200-402-A50), rabbit anti-mouse CD3 (clone SP7; Spring  
558 Bioscience Corp.), rabbit anti-mouse CD4 (clone #1; SinoBiological), rabbit anti-mouse CD8  
559 (D4W2Z; Cell Signaling Technology), rat anti-mouse CD45R (clone B220, BD Pharmingen),  
560 rabbit anti-human Iba1/AIF1 (Wako, 019-19741). Briefly, after deparaffination, sections  
561 underwent antigen retrieval in citrate buffer (pH 6.0; Agilent) (anti-SARS-CoV-2, -CD8, -CD45R,  
562 -Iba1) or Tris-EDTA buffer, pH 9.0 (anti-CD3, -CD4) for 20 min at 98 °C and for 20 min at 37 °C

563 respectively, followed by incubation with the primary antibody overnight at 4 °C (anti-SARS-  
564 CoV-2), 60 min at RT (anti-CD3, -CD8, -CD45R, -Iba1) or 60 min at 37 °C (anti-CD3, -CD4). This  
565 was followed by blocking of endogenous peroxidase (peroxidase block, Agilent) for 10 min at  
566 RT and incubation with the secondary antibody, EnVision+/HRP, Rabbit and Rat respectively  
567 (Agilent) for 30 min at RT (anti-SARS-CoV, -CD8, -CD45R, -Iba1) or the Omni-Map anti Rb HRP  
568 (Ventana) for 16 min at 37 °C (anti-CD3, -CD4), followed by EnVision FLEX DAB+ Chromogen in  
569 Substrate buffer (Agilent; anti-SARS-CoV-2, -CD8, -CD45R, -Iba1) for 10 min at RT or the DAB-  
570 Map-Kit (Ventana; anti-CD3, -CD4), all in an autostainer (Dako or Ventana). Sections were  
571 subsequently counterstained with haematoxylin.

572     **REFERENCES**

- 573     Aricescu, A.R., Lu, W., and Jones, E.Y. (2006). A time- and cost-efficient system for high-level  
574     protein production in mammalian cells. *Acta Crystallogr D Biol Crystallogr* *62*, 1243–1250.
- 575     Bischof, E., Wolfe, J., and Klein, S.L. (2020). Clinical trials for COVID-19 should include sex as a  
576     variable. *The Journal of Clinical Investigation* *130*, 3350–3352.
- 577     Bottermann, M., Foss, S., van Tienen, L.M., Vaysburd, M., Cruickshank, J., O’Connell, K., Clark,  
578     J., Mayes, K., Higginson, K., Hirst, J.C., et al. (2018). TRIM21 mediates antibody inhibition of  
579     adenovirus-based gene delivery and vaccination. *Proceedings of the National Academy of*  
580     *Sciences of the United States of America* *115*, 10440–10445.
- 581     Brune, K.D., and Howarth, M. (2018). New Routes and Opportunities for Modular Construction  
582     of Particulate Vaccines: Stick, Click, and Glue. *Frontiers in Immunology* *9*, 1432.
- 583     Bruun, T.U.J., Andersson, A.-M.C., Draper, S.J., and Howarth, M. (2018). Engineering a Rugged  
584     Nanoscaffold To Enhance Plug-and-Display Vaccination. *ACS Nano* *12*, 8855–8866.
- 585     Bussani, R., Schneider, E., Zentilin, L., Collesi, C., Ali, H., Braga, L., Volpe, M.C., Colliva, A.,  
586     Zanconati, F., Berlot, G., et al. (2020). Persistence of viral RNA, pneumocyte syncytia and  
587     thrombosis are hallmarks of advanced COVID-19 pathology. *EBioMedicine* *61*, 103104.
- 588     Chang, V.T., Spooner, R.A., Crispin, M., and Davis, S.J. (2015). Glycan Remodeling with  
589     Processing Inhibitors and Lectin-Resistant Eukaryotic Cells. *Methods in Molecular Biology*  
590     *1321*, 307–322.
- 591     Chang, V.T., Fernandes, R.A., Ganzinger, K.A., Lee, S.F., Siebold, C., McColl, J., Jonsson, P.,  
592     Palayret, M., Harlos, K., Coles, C.H., et al. (2016). Initiation of T cell signaling by CD45  
593     segregation at “close contacts.” *Nature Immunology* *17*, 574–582.
- 594     Chen, Z., and John Wherry, E. (2020). T cell responses in patients with COVID-19. *Nature*  
595     *Reviews. Immunology* *20*, 529–536.
- 596     Cohen, A.A., Gnanapragasam, P.N.P., Lee, Y.E., Hoffman, P.R., Ou, S., Kakutani, L.M., Keeffe,  
597     J.R., Wu, H.J., Howarth, M., West, A.P., et al. (2021). Mosaic nanoparticles elicit cross-reactive  
598     immune responses to zoonotic coronaviruses in mice. *Science* *371*, 735–741.
- 599     Cucinotta, D., and Vanelli, M. (2020). WHO Declares COVID-19 a Pandemic. *Acta Bio-Medica :*  
600     *Atenei Parmensis* *91*, 157–160.
- 601     Dalvie, N.C., Rodriguez-Aponte, S.A., Hartwell, B.L., Tostanoski, L.H., Biedermann, A.M.,  
602     Crowell, L.E., Kaur, K., Kumru, O., Carter, L., Yu, J., et al. (2021). Engineered SARS-CoV-2  
603     receptor binding domain improves immunogenicity in mice and elicits protective immunity in  
604     hamsters. *BioRxiv* 2021.03.03.433558.
- 605     Davidson, A.D., Williamson, M.K., Lewis, S., Shoemark, D., Carroll, M.W., Heesom, K.J., Zambon,  
606     M., Ellis, J., Lewis, P.A., Hiscox, J.A., et al. (2020). Characterisation of the transcriptome and

- 607 proteome of SARS-CoV-2 reveals a cell passage induced in-frame deletion of the furin-like  
608 cleavage site from the spike glycoprotein. *Genome Medicine* *12*, 68.
- 609 Davies, N.G., Abbott, S., Barnard, R.C., Jarvis, C.I., Kucharski, A.J., Munday, J.D., Pearson, C.A.B.,  
610 Russell, T.W., Tully, D.C., Washburne, A.D., et al. (2021). Estimated transmissibility and impact  
611 of SARS-CoV-2 lineage B.1.1.7 in England. *Science* *372*.
- 612 Elegheert, J., Behiels, E., Bishop, B., Scott, S., Woolley, R.E., Griffiths, S.C., Byrne, E.F.X., Chang,  
613 V.T., Stuart, D.I., Jones, E.Y., et al. (2018). Lentiviral transduction of mammalian cells for fast,  
614 scalable and high-level production of soluble and membrane proteins. *Nature Protocols* *13*,  
615 2991–3017.
- 616 Ferreira, I., Datir, R., Papa, G., Kemp, S., Meng, B., Rakshit, P., Singh, S., Pandey, R., Ponnusamy,  
617 K., Radhakrishnan, V.S., et al. (2021). SARS-CoV-2 B.1.617 emergence and sensitivity to vaccine-  
618 elicited antibodies. *BioRxiv* 2021.05.08.443253.
- 619 Gauss, G.H., Benas, P., Wiedenheft, B., Young, M., Douglas, T., and Lawrence, C.M. (2006).  
620 Structure of the DPS-like protein from *Sulfolobus solfataricus* reveals a bacterioferritin-like  
621 dimetal binding site within a DPS-like dodecameric assembly. *Biochemistry* *45*, 10815–10827.
- 622 Gu, M., Torres, J.L., Greenhouse, J., Wallace, S., Chiang, C.-I., Jackson, A.M., Porto, M., Kar, S.,  
623 Li, Y., Ward, A.B., et al. (2021). One dose of COVID-19 nanoparticle vaccine REVC-128 provides  
624 protection against SARS-CoV-2 challenge at two weeks post immunization. *BioRxiv*  
625 2021.04.02.438218.
- 626 He, L., Lin, X., Wang, Y., Abraham, C., Sou, C., Ngo, T., Zhang, Y., Wilson, I.A., and Zhu, J. (2021).  
627 Single-component, self-assembling, protein nanoparticles presenting the receptor binding  
628 domain and stabilized spike as SARS-CoV-2 vaccine candidates. *Science Advances* *7*.
- 629 Hsia, Y., Bale, J.B., Gonen, S., Shi, D., Sheffler, W., Fong, K.K., Nattermann, U., Xu, C., Huang,  
630 P.S., Ravichandran, R., et al. (2016). Design of a hyperstable 60-subunit protein dodecahedron.  
631 [corrected]. *Nature* *535*, 136–139.
- 632 Huang, Y., Yang, C., Xu, X.F., Xu, W., and Liu, S.W. (2020). Structural and functional properties  
633 of SARS-CoV-2 spike protein: potential antiviral drug development for COVID-19. *Acta*  
634 *Pharmacologica Sinica* *41*, 1141–1149.
- 635 Joyce, M.G., King, H.A.D., Naouar, I.E., Ahmed, A., Peachman, K.K., Cincotta, C.M., Subra, C.,  
636 Chen, R.E., Thomas, P.V., Chen, W.H., et al. (2021). Efficacy of a Broadly Neutralizing SARS-CoV-  
637 2 Ferritin Nanoparticle Vaccine in Nonhuman Primates. *BioRxiv : The Preprint Server for*  
638 *Biology*.
- 639 Kalathiya, U., Padariya, M., Fahraeus, R., Chakraborti, S., and Hupp, T.R. (2021). Multivalent  
640 Display of SARS-CoV-2 Spike (RBD Domain) of COVID-19 to Nanomaterial, Protein Ferritin  
641 Nanocages. *Biomolecules* *11*.
- 642 Kato, Y., Abbott, R.K., Freeman, B.L., Haupt, S., Groschel, B., Silva, M., Menis, S., Irvine, D.J.,  
643 Schief, W.R., and Crotty, S. (2020). Multifaceted Effects of Antigen Valency on B Cell Response  
644 Composition and Differentiation In Vivo. *Immunity* *53*, 548-563 e8.

- 645 Ke, Z., Oton, J., Qu, K., Cortese, M., Zila, V., McKeane, L., Nakane, T., Zivanov, J., Neufeldt, C.J.,  
646 Cerikan, B., et al. (2020). Structures and distributions of SARS-CoV-2 spike proteins on intact  
647 virions. *Nature* 588, 498–502.
- 648 Klein, S.L., Dhakal, S., Ursin, R.L., Deshpande, S., Sandberg, K., and Mauvais-Jarvis, F. (2020).  
649 Biological sex impacts COVID-19 outcomes. *PLoS Pathogens* 16, e1008570.
- 650 Koenig, P.A., Das, H., Liu, H., Kummerer, B.M., Gohr, F.N., Jenster, L.M., Schiffelers, L.D.J.,  
651 Tesfamariam, Y.M., Uchima, M., Wuerth, J.D., et al. (2021). Structure-guided multivalent  
652 nanobodies block SARS-CoV-2 infection and suppress mutational escape. *Science* 371.
- 653 Kupferschmidt, K. (2021). New mutations raise specter of “immune escape.” *Science* 371, 329–  
654 330.
- 655 Liu, Z., Xu, W., Xia, S., Gu, C., Wang, X., Wang, Q., Zhou, J., Wu, Y., Cai, X., Qu, D., et al. (2020).  
656 RBD-Fc-based COVID-19 vaccine candidate induces highly potent SARS-CoV-2 neutralizing  
657 antibody response. *Signal Transduction and Targeted Therapy* 5, 282.
- 658 Ma, X., Zou, F., Yu, F., Li, R., Yuan, Y., Zhang, Y., Zhang, X., Deng, J., Chen, T., Song, Z., et al.  
659 (2020). Nanoparticle Vaccines Based on the Receptor Binding Domain (RBD) and Heptad  
660 Repeat (HR) of SARS-CoV-2 Elicit Robust Protective Immune Responses. *Immunity* 53, 1315-  
661 1330 e9.
- 662 Mahase, E. (2020). Covid-19: What do we know about the late stage vaccine candidates? *Bmj*  
663 371, m4576.
- 664 Mahase, E. (2021). Covid-19: Novavax vaccine efficacy is 86% against UK variant and 60%  
665 against South African variant. *Bmj* 372, n296.
- 666 Morecroft, J.A., and Thomas, M.H. (1988). Radionuclide ejection fraction. *The British Journal*  
667 *of Surgery* 75, 188.
- 668 Nelde, A., Bilich, T., Heitmann, J.S., Maringer, Y., Salih, H.R., Roerden, M., Lubke, M., Bauer, J.,  
669 Rieth, J., Wacker, M., et al. (2021). SARS-CoV-2-derived peptides define heterologous and  
670 COVID-19-induced T cell recognition. *Nature Immunology* 22, 74–85.
- 671 Pal, M., Berhanu, G., Desalegn, C., and Kandi, V. (2020). Severe Acute Respiratory Syndrome  
672 Coronavirus-2 (SARS-CoV-2): An Update. *Cureus* 12, e7423.
- 673 Papa, G., Mallery, D.L., Albecka, A., Welch, L.G., Cattin-Ortola, J., Luptak, J., Paul, D., McMahon,  
674 H.T., Goodfellow, I.G., Carter, A., et al. (2021). Furin cleavage of SARS-CoV-2 Spike promotes  
675 but is not essential for infection and cell-cell fusion. *PLoS Pathogens* 17, e1009246.
- 676 Patterson, E.I., Prince, T., Anderson, E.R., Casas-Sanchez, A., Smith, S.L., Cansado-Utrilla, C.,  
677 Solomon, T., Griffiths, M.J., Acosta-Serrano, A., Turtle, L., et al. (2020). Methods of Inactivation  
678 of SARS-CoV-2 for Downstream Biological Assays. *The Journal of Infectious Diseases* 222, 1462–  
679 1467.

- 680 Pickering, S., Betancor, G., Galao, R.P., Merrick, B., Signell, A.W., Wilson, H.D., Kia Ik, M.T.,  
681 Seow, J., Graham, C., Acors, S., et al. (2020). Comparative assessment of multiple COVID-19  
682 serological technologies supports continued evaluation of point-of-care lateral flow assays in  
683 hospital and community healthcare settings. *PLoS Pathogens* *16*, e1008817.
- 684 Pollet, J., Chen, W.H., and Strych, U. (2021). Recombinant protein vaccines, a proven approach  
685 against coronavirus pandemics. *Advanced Drug Delivery Reviews* *170*, 71–82.
- 686 Powell, A.E., Zhang, K., Sanyal, M., Tang, S., Weidenbacher, P.A., Li, S., Pham, T.D., Pak, J.E.,  
687 Chiu, W., and Kim, P.S. (2021). A Single Immunization with Spike-Functionalized Ferritin  
688 Vaccines Elicits Neutralizing Antibody Responses against SARS-CoV-2 in Mice. *ACS Central*  
689 *Science* *7*, 183–199.
- 690 Sauer, K., and Harris, T. (2020). An Effective COVID-19 Vaccine Needs to Engage T Cells.  
691 *Frontiers in Immunology* *11*, 581807.
- 692 Schurink, B., Roos, E., Radonic, T., Barbe, E., Bouman, C.S.C., de Boer, H.H., de Bree, G.J., Bulle,  
693 E.B., Aronica, E.M., Florquin, S., et al. (2020). Viral presence and immunopathology in patients  
694 with lethal COVID-19: a prospective autopsy cohort study. *The Lancet. Microbe* *1*, e290–e299.
- 695 Scully, E.P., Haverfield, J., Ursin, R.L., Tannenbaum, C., and Klein, S.L. (2020). Considering how  
696 biological sex impacts immune responses and COVID-19 outcomes. *Nature Reviews.*  
697 *Immunology* *20*, 442–447.
- 698 Seydoux, E., Homad, L.J., MacCamy, A.J., Parks, K.R., Hurlburt, N.K., Jennewein, M.F., Akins,  
699 N.R., Stuart, A.B., Wan, Y.H., Feng, J., et al. (2020). Characterization of neutralizing antibodies  
700 from a SARS-CoV-2 infected individual. *BioRxiv : The Preprint Server for Biology*.
- 701 Shang, J., Wan, Y., Luo, C., Ye, G., Geng, Q., Auerbach, A., and Li, F. (2020). Cell entry  
702 mechanisms of SARS-CoV-2. *Proceedings of the National Academy of Sciences of the United*  
703 *States of America* *117*, 11727–11734.
- 704 Tan, T.K., Rijal, P., Rahikainen, R., Keeble, A.H., Schimanski, L., Hussain, S., Harvey, R., Hayes,  
705 J.W.P., Edwards, J.C., McLean, R.K., et al. (2021). A COVID-19 vaccine candidate using  
706 SpyCatcher multimerization of the SARS-CoV-2 spike protein receptor-binding domain induces  
707 potent neutralising antibody responses. *Nature Communications* *12*, 542.
- 708 Thompson, M.G., Burgess, J.L., Naleway, A.L., Tyner, H.L., Yoon, S.K., Meece, J., Olsho, L.E.W.,  
709 Caban-Martinez, A.J., Fowlkes, A., Lutrick, K., et al. (2021). Interim Estimates of Vaccine  
710 Effectiveness of BNT162b2 and mRNA-1273 COVID-19 Vaccines in Preventing SARS-CoV-2  
711 Infection Among Health Care Personnel, First Responders, and Other Essential and Frontline  
712 Workers - Eight U.S. Locations, December 2020-March 2021. *MMWR. Morbidity and Mortality*  
713 *Weekly Report* *70*, 495–500.
- 714 Walls, A.C., Fiala, B., Schafer, A., Wrenn, S., Pham, M.N., Murphy, M., Tse, L.V., Shehata, L.,  
715 O'Connor, M.A., Chen, C., et al. (2020). Elicitation of Potent Neutralizing Antibody Responses  
716 by Designed Protein Nanoparticle Vaccines for SARS-CoV-2. *Cell* *183*, 1367-1382 e17.



- 717 Wang, W., Huang, B., Zhu, Y., Tan, W., and Zhu, M. (2021). Ferritin nanoparticle-based SARS-  
718 CoV-2 RBD vaccine induces a persistent antibody response and long-term memory in mice.  
719 *Cellular & Molecular Immunology* *18*, 749–751.
- 720 Wölfel, R., Corman, V.M., Guggemos, W., Seilmaier, M., Zange, S., Müller, M.A., Niemeyer, D.,  
721 Jones, T.C., Vollmar, P., Rothe, C., et al. (2020). Virological assessment of hospitalized patients  
722 with COVID-2019. *Nature* *581*, 465–469.
- 723 Wrapp, D., Wang, N., Corbett, K.S., Goldsmith, J.A., Hsieh, C.L., Abiona, O., Graham, B.S., and  
724 McLellan, J.S. (2020). Cryo-EM structure of the 2019-nCoV spike in the prefusion conformation.  
725 *Science* *367*, 1260–1263.
- 726 Xiang, Y., Nambulli, S., Xiao, Z., Liu, H., Sang, Z., Duprex, W.P., Schneidman-Duhovny, D., Zhang,  
727 C., and Shi, Y. (2020). Versatile and multivalent nanobodies efficiently neutralize SARS-CoV-2.  
728 *Science* *370*, 1479–1484.
- 729 Yang, J., Wang, W., Chen, Z., Lu, S., Yang, F., Bi, Z., Bao, L., Mo, F., Li, X., Huang, Y., et al. (2020).  
730 A vaccine targeting the RBD of the S protein of SARS-CoV-2 induces protective immunity.  
731 *Nature* *586*, 572–577.
- 732 Zakeri, B., Fierer, J.O., Celik, E., Chittock, E.C., Schwarz-Linek, U., Moy, V.T., and Howarth, M.  
733 (2012). Peptide tag forming a rapid covalent bond to a protein, through engineering a bacterial  
734 adhesin. *Proceedings of the National Academy of Sciences of the United States of America* *109*,  
735 E690-7.
- 736 Zeng, W., Liu, G., Ma, H., Zhao, D., Yang, Y., Liu, M., Mohammed, A., Zhao, C., Yang, Y., Xie, J.,  
737 et al. (2020). Biochemical characterization of SARS-CoV-2 nucleocapsid protein. *Biochemical*  
738 *and Biophysical Research Communications* *527*, 618–623.
- 739 Zhang, W., Davis, B.D., Chen, S.S., Sincuir Martinez, J.M., Plummer, J.T., and Vail, E. (2021).  
740 Emergence of a Novel SARS-CoV-2 Variant in Southern California. *Jama* *325*, 1324–1326.
- 741 Zheng, J., Wong, L.R., Li, K., Verma, A.K., Ortiz, M.E., Wohlford-Lenane, C., Leidinger, M.R.,  
742 Knudson, C.M., Meyerholz, D.K., McCray, P.B., Jr., et al. (2021). COVID-19 treatments and  
743 pathogenesis including anosmia in K18-hACE2 mice. *Nature* *589*, 603–607.
- 744 Zuo, J., Dowell, A.C., Pearce, H., Verma, K., Long, H.M., Begum, J., Aiano, F., Amin-Chowdhury,  
745 Z., Hallis, B., Stapley, L., et al. (2021). Robust SARS-CoV-2-specific T cell immunity is maintained  
746 at 6 months following primary infection. *Nature Immunology*.
- 747 (2021a). The New York Times, Coronavirus Vaccine Tracker (The New York Times).
- 748 (2021b). World Health Organization, COVID-19 situation reports.
- 749



750 **ACKNOWLEDGEMENTS**

751 We thank Mark Wing and Kevin O'Connell (MRC-LMB, Cambridge). We would especially like to  
752 thank the biomedical research staff at Liverpool and the LMB's Ares facility for their help and  
753 support, as well as the technical staff of the Histology Laboratory, Institute of Veterinary  
754 Pathology, Vetsuisse Faculty Zurich. Work at the MRC-LMB was funded by the Medical  
755 Research Council, UK (U105184326 to JL, U105181010 to LCJ, MC\_UP\_1201/15 and  
756 MR/L009609/1 to ARA) and Wellcome, UK (203276/C/16/Z to JL, 200594/Z/16/Z and  
757 214344/A/18/Z to LCJ). Work in Liverpool was funded in by the Medical Research Council, UK  
758 (MR/W005611/1 to JPS and JAH) and the US Food and Drug Administration, USA  
759 (75F40120C00085 to JAH).

760

761 **CONFLICTS OF INTEREST**

762 The authors declare no competing interests.

763 **FIGURE LEGENDS**

764 **Figure 1. Overview of the multimerisation strategy employed and the antigens and scaffold**  
765 **used.** **A)** Cartoon representation of SARS-CoV-2 binding to a human cell membrane. **B)**  
766 Schematic diagram of the *Sulfolobus islandicus* Dps and SpyCatcher-based display and  
767 multimerisation strategy employed in this study. **C)** Diagram of the proteins used in this work.  
768 SpyC is the  $\Delta$ N1-SpyCatcher domain and SpyT2 is the peptidic SpyTag2 that becomes covalently  
769 linked to SpyC upon simple mixing. Stabilised, trimeric Spike/Spike-SpyT2 contained on  
770 average only one SpyT2 tag in order to avoid uncontrolled oligomerisation when coupled to  
771 Dps.

772 **Figure 2: Preparation and quality control of coupled antigen – Dps complexes (Ag-S-Dps).** **A)**  
773 SDS-PAGE of the three expressed and purified antigens as introduced in Fig. 1C. Glycosylation  
774 of Spike leads to a fuzzy appearance of its band. RBD-SpyT2 and Spike-SpyT2 were expressed  
775 in mammalian cells, SpyT2-NP was expressed in bacteria, as was the SpyC-Dps scaffold. **B)** Size-  
776 exclusion chromatography to separate excess antigens after the SpyCatcher/Spytag2 coupling  
777 reactions; Superose 6 Increase in PBS. **C)** SDS-PAGE of the coupled and purified Ag-S-Dps  
778 complexes. “RT”, no heating; “99”, heated to 99°C. The SpyC-Dps scaffold alone, as well as all  
779 the three coupled complexes show high-molecular weight complexes, presumably  
780 dodecameric, that disappear only after heating of the samples in SDS loading buffer. **D)**  
781 Negative-stain electron microscopy analyses of the three multimeric Ag-S-Dps complexes,  
782 showing that all samples form defined and monodisperse spheres that display the antigens on  
783 their surface, leading to particles of different sizes for the three differently-sized antigens.

784 **Figure 3: Mouse immunisation – multimeric Ag-S-Dps complexes elicit a powerful and**  
785 **neutralising antibody response in mice.** **A)** Immunisation protocol. **B)** Bleeds on day 34 and 74  
786 were tested for binding activity by ELISA against Spike-SpyT2, NP-SpyT2 or polymeric scaffold,  
787 SpyC-Dps. In all cases did the multimerised Ag-S-Dps complexes produce more antibodies than  
788 the non-multimerised versions. RBD-S-Dps and NP-S-Dps produced very strong responses. **C)**  
789 Pseudoviral cell entry neutralisation assay with sera from the 2<sup>nd</sup> bleed. Sera from immunised  
790 mice were tested for neutralisation activity against a Spike-pseudotyped lentiviral GFP vector  
791 (hence NP-S-Dps sera will not neutralise). Relative infection is plotted 72 hrs after vector  
792 addition by quantifying GFP expression in HEK 293T ACE2/TMPRSS2 target cells. The

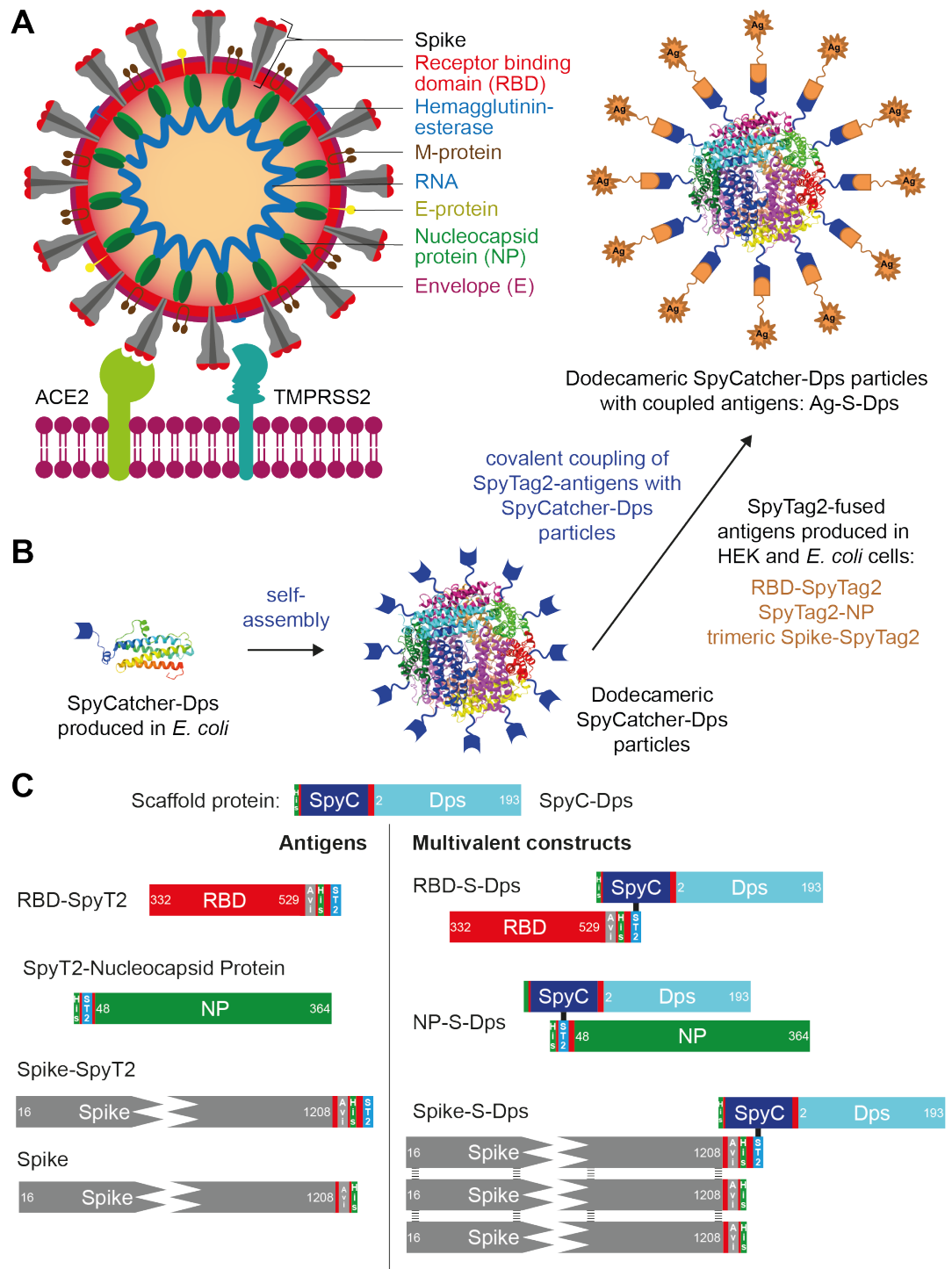
793 multimerised RBD-S-Dps and Spike-S-Dps showed strong neutralisation, in contrast to their  
794 non-multimerised precursors. **D)** Same as C) but using sera from the 3<sup>rd</sup> bleed. Neutralisation  
795 activity is enhanced in all sera, and the differential between multimerised and non-  
796 multimerised antigens remains. Overall, RBD-S-Dps showed the strongest neutralisation  
797 activity.

798 **Figure 4: Single-shot immunisation and Sars-CoV-2 challenge experiment using hACE2-mice.**

799 **A)** Immunisation and challenge protocol. **B)** K18-hACE2 mice were immunised with 25 µg of  
800 RBD-S-Dps, RBD-SpyT2 or given PBS, plus 10 µg CpG adjuvant. The animals were challenged on  
801 day 28 with 10<sup>4</sup> PFU SARS-CoV-2 and changes in weight recorded. The animals in the PBS  
802 control group and those who had been given RBD-SpyT2 showed the characteristic weight loss  
803 after four days post infection. RBD-S-Dps-immunised mice showed no such weight loss. **C)** Two-  
804 way ANOVA tests on the weight changes between groups, as plotted in B). **D)** Sera from days  
805 13, 24 and 35 were tested for anti-RBD antibodies by ELISA. Only RBD-S-Dps mice showed  
806 significant antibody. **E)** Plaque assay using lung homogenates from mice culled seven days  
807 post-infection. RBD-S-Dps-immunised mice contained very low amounts of infectious SARS-  
808 CoV-2 in their lungs. **F) and G)** Genomic and subgenomic (gRNA, sgRNA) qPCR on RNA extracted  
809 from lung homogenates, using probes against NP or E, respectively. Two-way ANOVA tests  
810 were carried out with significance levels of:  $p = < 0.05$  (\*),  $p = < 0.05$  (\*\*),  $p = < 0.005$  (\*\*\*),  $p$   
811  $= < 0.0005$  (\*\*\*\*). **H)** Representative lung sections from animals (n=6) taken seven days post-  
812 challenge, stained by immunohistology for SARS-CoV-2 NP protein.

813 FIGURES

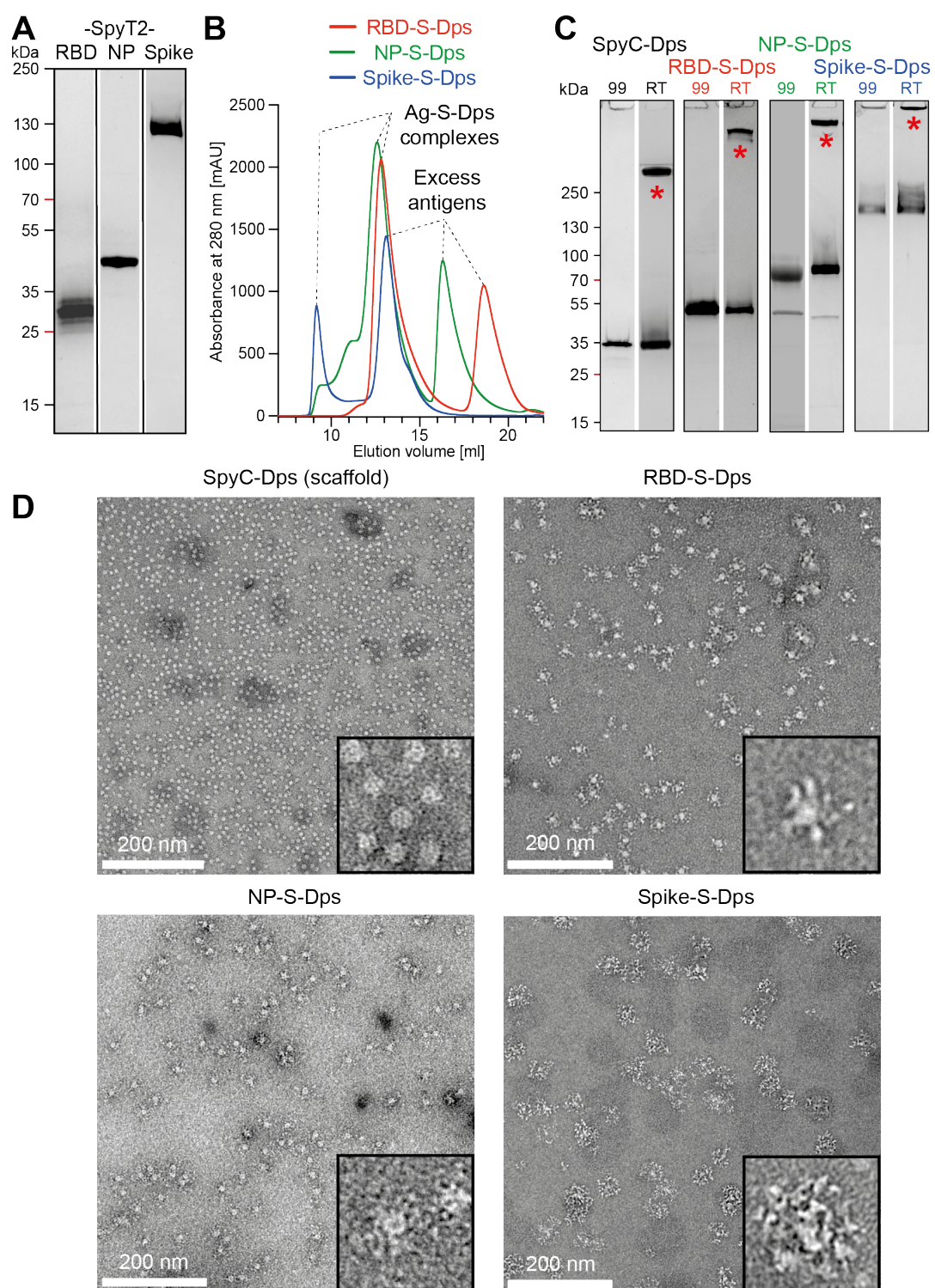
814 Figure 1



815

816

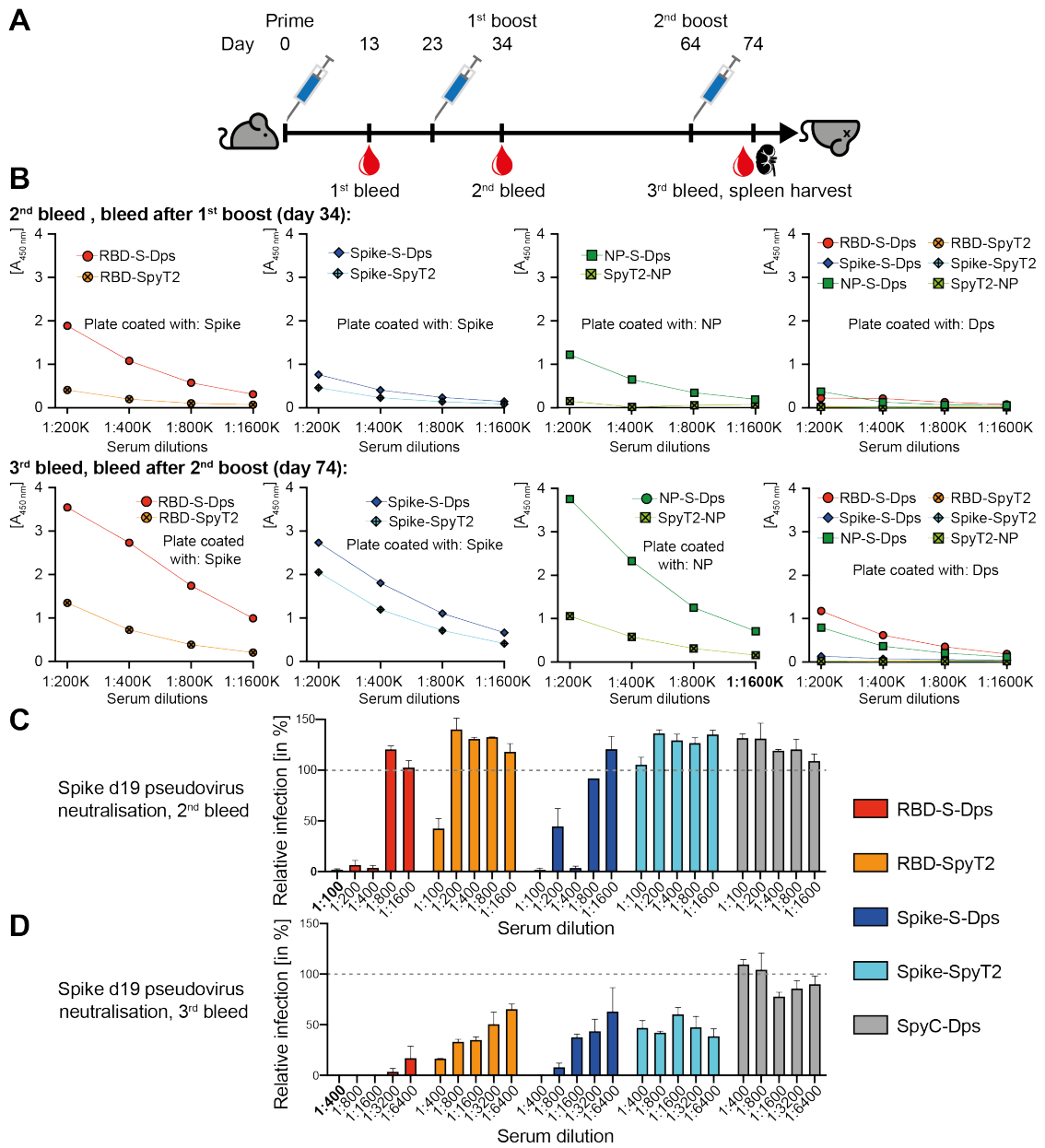
817 **Figure 2**



818



819 **Figure 3**



820

821



824 **SUPPLEMENTAL INFORMATION**

825 **SUPPLEMENTAL RESULTS**

826 Detailed description of the lung histology in RBS-D-Dps-immunised mice subsequently  
827 challenged with SARS-Cov-2 (Fig. 4A):

828 **Mice immunised with PBS control.** All animals showed a mild to moderate increase in  
829 interstitial cellularity and multifocal extensive areas of consolidation due to macrophage and  
830 lymphocyte infiltration, with a few neutrophils and with abundant activated type II cells,  
831 occasional syncytial cells and some degenerate cells and moderate mesothelial cell activation  
832 above the affected parenchymal area (Suppl. Fig. 4A). The changes were associated with  
833 extensive viral antigen expression in type I and type II pneumocytes both in consolidated areas  
834 and in alveoli without inflammatory changes. Occasional macrophages in the infiltrate also  
835 appeared to express viral antigen (Suppl. Fig. 4B). Macrophages (Iba1+) were the dominant  
836 cells in the infiltrates (Suppl. Fig. 5A), followed by numerous T cells with a relatively high  
837 proportion and CD4 positive cells and less CD8 positive cells (Suppl. Fig. 5C, E, G), and a  
838 moderate number of B cells (Suppl. Fig. 5I). There were also areas where alveoli exhibited type  
839 II cell activation and desquamation, with desquamation of alveolar macrophages and some  
840 neutrophils in the lumen. In addition, mild to moderate mononuclear vasculitis (mainly  
841 arteritis) was seen (Suppl. Fig. 4A). Also, the infiltrate was dominated by macrophages,  
842 followed by T cells (CD4 positive cells and less CD8 positive cells) and fewer B cells.

843 **Mice immunised with monomeric RBD-SpyT2.** All animals showed a mild to moderate  
844 increase in interstitial cellularity and multifocal extensive areas of consolidation similar in  
845 composition and extent to those seen in the PBS-control mice (Suppl. Fig. 4C). Viral antigen  
846 was detected in multiple variably-sized foci, in type I and II pneumocytes and in macrophages  
847 within and close to consolidated areas (Suppl. Fig. 4D).

848 **Mice immunised with multimerised RBD-S-Dps.** The three female animals showed minimal  
849 histological changes in the lungs (Suppl. Fig. 4E). Besides a very mild increase in interstitial  
850 cellularity, with rare T cells (both CD4 and CD8 positive cells) and B cells, one animal showed  
851 scattered small focal leukocyte aggregates. Viral antigen expression was restricted to a few  
852 macrophages in the leukocyte aggregates in the latter animal, while a second had positive

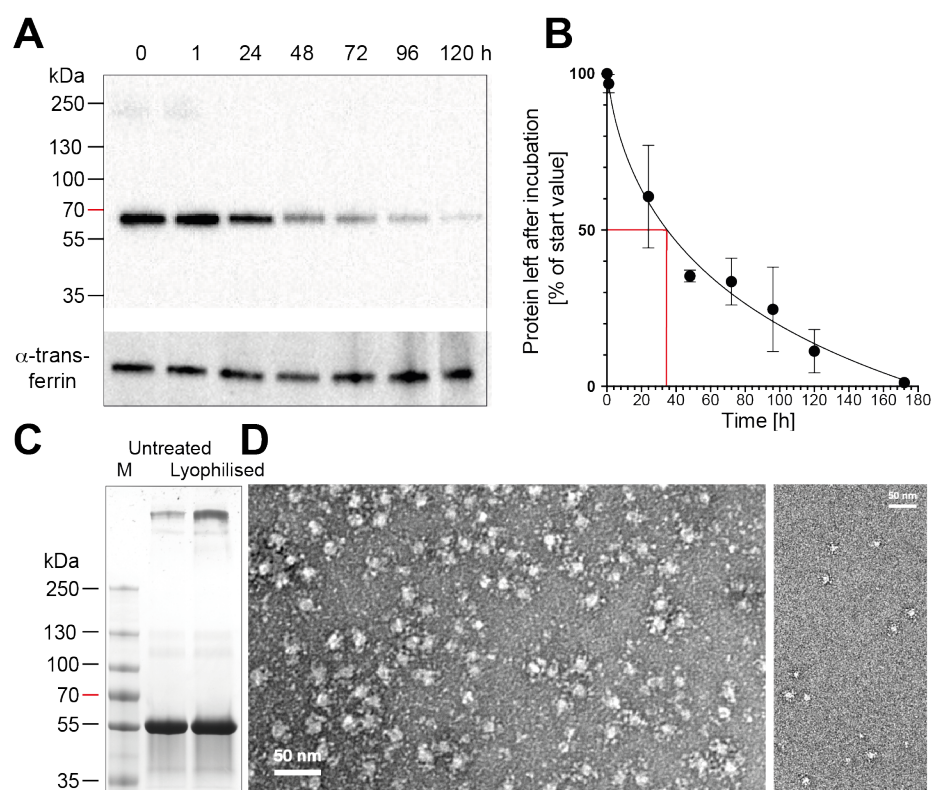


853 pneumocyte in an alveolus; in the third lung, viral antigen was not detected (Suppl. Fig. 4F). In  
854 male animals, multifocal inflammatory infiltrates with viral antigen expression and mild  
855 vasculitis similar to the other two groups, but substantially less extensive were seen (Suppl.  
856 Fig. 4G, H). Also here, macrophages were the dominant cells in the focal infiltrates (Suppl. Fig.  
857 5B), followed by the T cells (Suppl. Fig. 5D). The T cell population showed a mild shift in  
858 composition, as now CD8-positive cells were as numerous or more frequent than CD4-positive  
859 cells (Suppl. Fig. 5F-H). CD8-positive cells were also seen within alveolar lumina (Suppl. Fig. 5B  
860 inset). B cells were found in moderate numbers in the infiltrates, in one animal they also  
861 formed peribronchiolar aggregates (Suppl. Fig. 5J).

862

863 **SUPPLEMENTAL FIGURES & TABLES**

864 **Supplemental Figure 1**

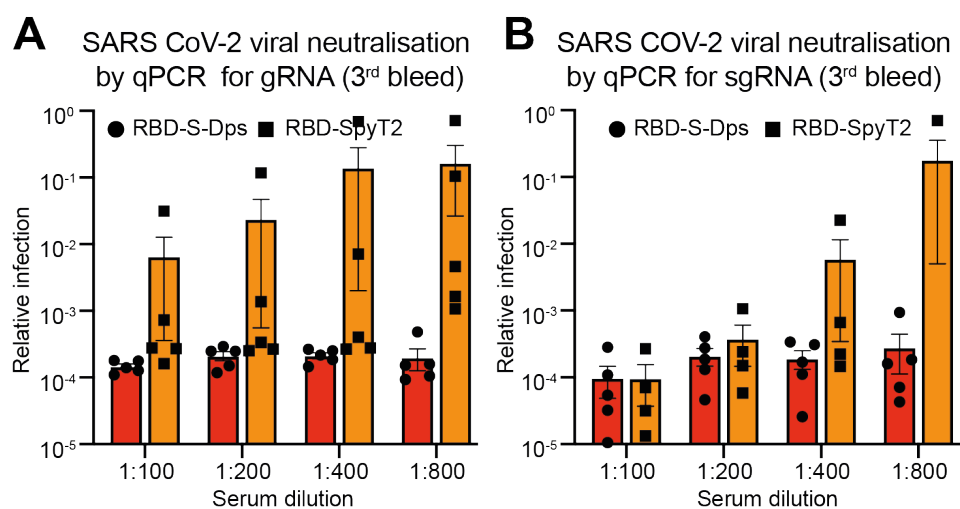


865

866 **A)** Plasma stability assay. RBD-S-Dps was incubated with non-heated human blood plasma for  
867 the amount of time indicated. SDS-PAGE and Western blot against the histidine tag on the  
868 protein. Transferrin was used as loading control and also detected by Western blot. **B)**  
869 Quantification of the data in A). The red line indicates the half-life of RBD-S-Dps under the  
870 conditions used. **C)** SDS-PAGE of RBD-S-Dps before and after lyophilisation. (Coomassie  
871 staining). **D)** The lyophilised sample from C) was diluted to two different concentrations to  
872 demonstrate monodispersity and subjected to negative stain electron microscopy (left 20 x  
873 dilution and right 100 x dilution).

874

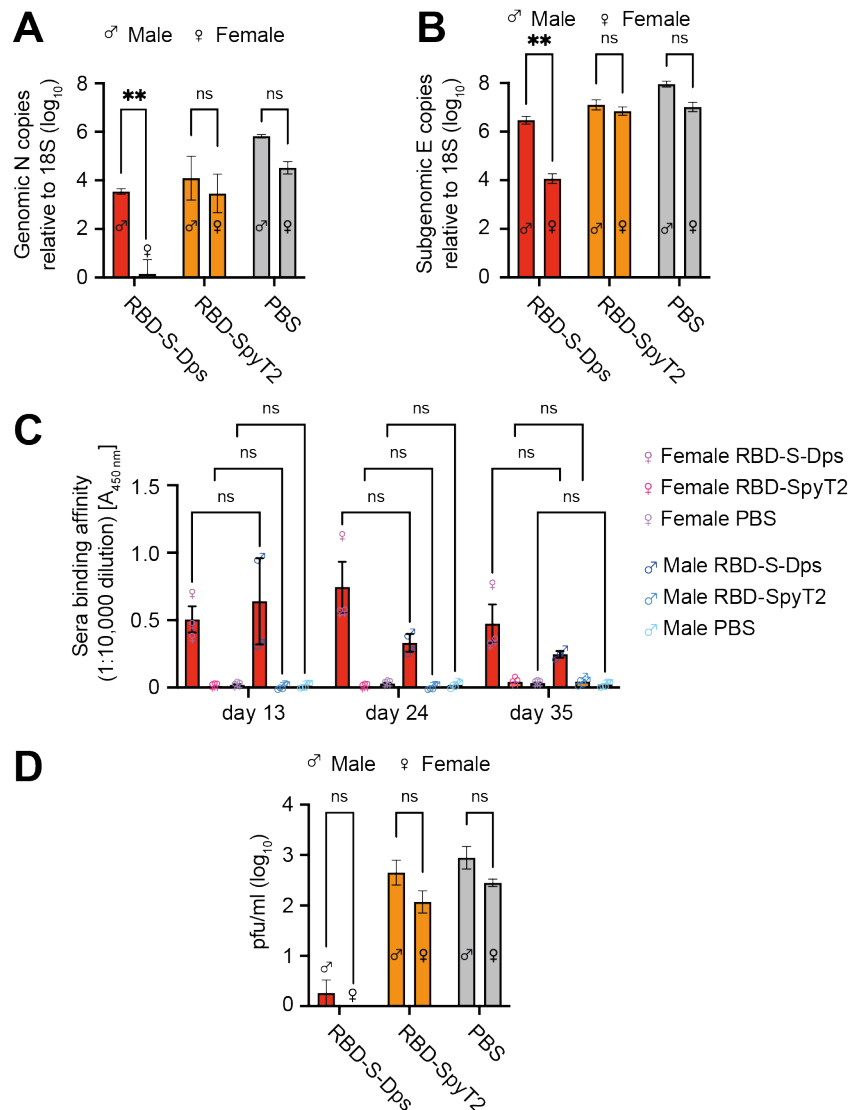
875 **Supplemental Figure 2**



876

877 **A, B):** Vero cells expressing ACE2 and TMPRSS2 were infected with SARS-CoV-2 in the presence  
878 of serial dilutions of antisera. Viral replication was then determined after 24 h by RT-qPCR using  
879 probes for gRNA (**A**) or sgRNA (**B**). Each point represents sera from an individual mouse.

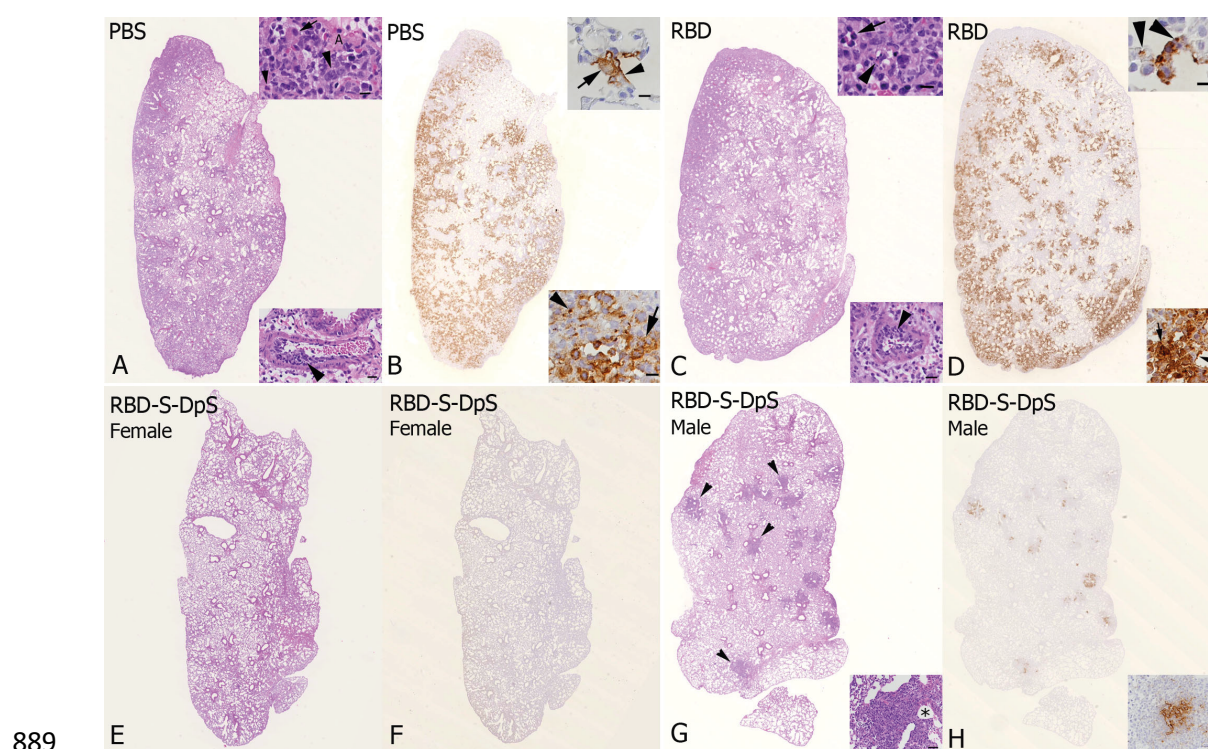
880 **Supplemental Figure 3**



881

882 Mice were immunised with RBD-S-Dps, RBD-SpyT2 or given PBS control on day 1 and then  
 883 challenged with SARS-CoV-2 on day 28. **A & B**) Genomic and subgenomic (gRNA, sgRNA) qPCR  
 884 on RNA extracted from lung homogenates, using probes against NP or E, respectively. **C**) Sera  
 885 from days 13, 24 and 35 were tested for anti-RBD antibodies by ELISA. Two-way ANOVA tests  
 886 show that there are non-significant differences between male and female antibody responses.  
 887 **D**) Plaque assay using lung homogenates from mice culled seven days post-infection.

888 **Supplemental Figure 4**

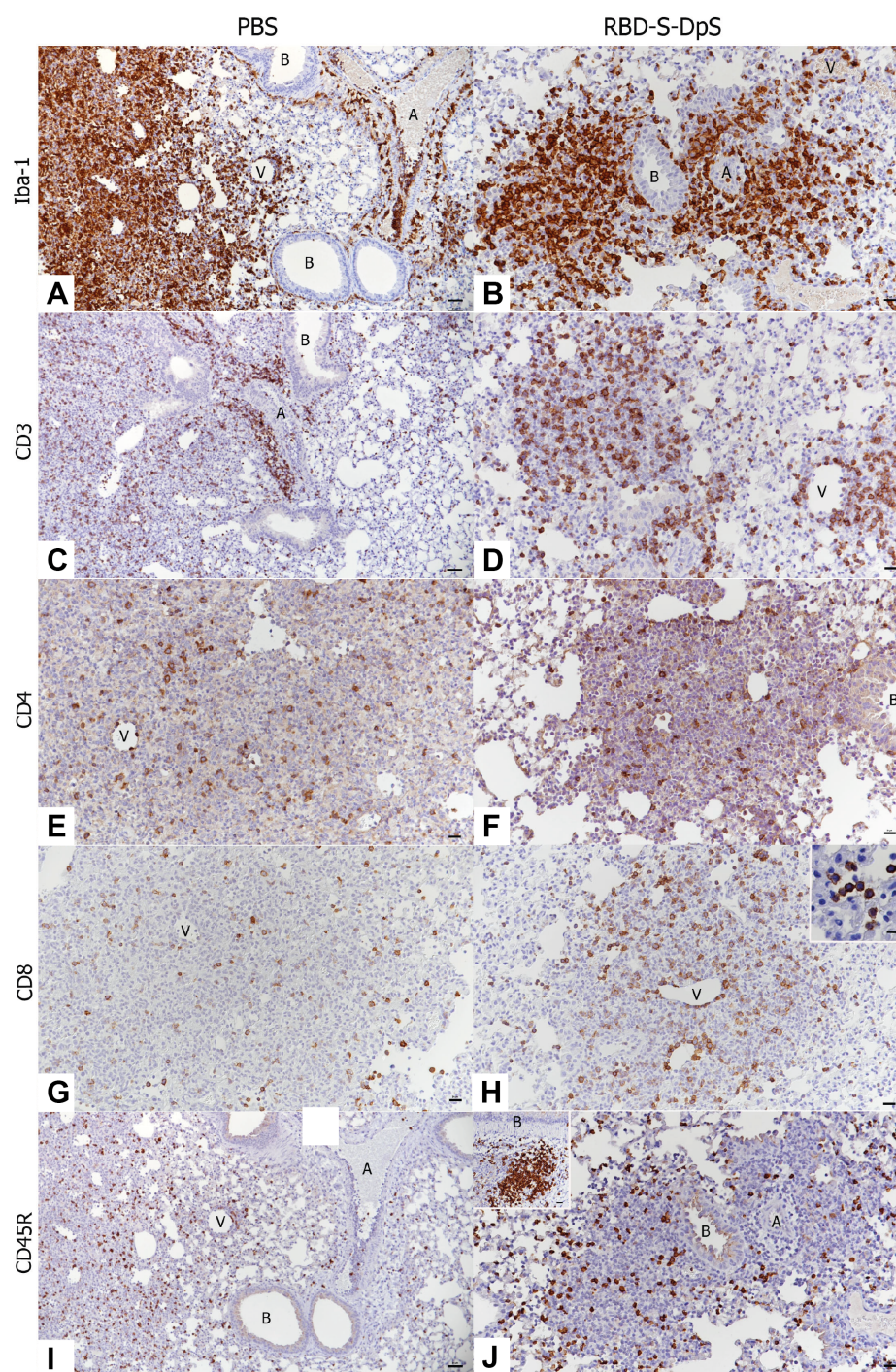


890 Lung, left lobe, K18-hACE2 mice at day seven post infection, SARS-CoV-2 challenge experiment.  
891 Histological changes and SARS-CoV-2 antigen expression. **A, B: mice injected with PBS control.**  
892 **A)** Overview of the lung lobe, with multifocal extensive cell-rich consolidated areas. Inset top:  
893 consolidated area with activated type II pneumocyte (small arrow), syncytial cells (large  
894 arrowhead) and infiltrating neutrophil (small arrowhead); A – alveolus (bar = 10  $\mu$ m). Inset  
895 bottom: artery with leukocyte infiltration of the wall (arrowhead; arteritis, bar = 20  $\mu$ m). HE  
896 stain. **B)** Extensive SARS-CoV-2 antigen expression is seen in multifocal patchy areas within  
897 and close to consolidated areas, in pneumocytes and occasional macrophages. Inset top:  
898 alveolus with viral antigen expression in type I (arrowhead) and type II (arrow) pneumocyte. Inset  
899 bottom: consolidated area with viral antigen expression in macrophages (arrow) and  
900 degenerate cells (arrowhead). Immunohistology, haematoxylin counterstain, bars = 10  $\mu$ m. **C,**  
901 **D: Monomeric RBD-SpyT2-immunised mice. C)** Overview of the lung lobe, with multifocal  
902 extensive cell-rich consolidated areas. Inset top: consolidated area with several neutrophils  
903 (arrowhead) and occasional necrotic cells (arrowhead, bar = 10  $\mu$ m). Inset bottom: artery with  
904 leukocyte infiltration of the wall (arrowhead; arteritis) and mild periarterial edema (bar = 20  
905  $\mu$ m). HE stain. **D)** Extensive SARS-CoV-2 antigen expression in multifocal patchy areas within

906 and close to consolidated areas, in pneumocytes and occasional macrophages. Inset top:  
907 alveolus with viral antigen expression in pneumocytes of which some are degenerate  
908 (arrowheads). Inset bottom: consolidated area with viral antigen expression in macrophages  
909 (arrow) and type I pneumocyte (arrowhead). Immunohistology, haematoxylin counterstain;  
910 bars = 10  $\mu\text{m}$ . **E-H: Multimerised RBD-S-Dps immunised mice. E, F. Female animal. E)** Overview  
911 of the lung lobe. The histological changes are restricted to focal areas of mildly increased  
912 interstitial cellularity. HE stain. **F)** There is no evidence of viral antigen expression.  
913 Immunohistology, haematoxylin counterstain. **G, H. Male animal. G)** Overview of the lung lobe,  
914 with several small, randomly distributed peribronchiolar cell-rich areas (arrowheads). Inset:  
915 Closer view of focal cell rich area (asterisk: bronchiole); bar = 50  $\mu\text{m}$ , HE stain. **H)** SARS-CoV-2  
916 antigen expression is restricted to the cell rich focal areas, in pneumocytes and occasional  
917 macrophages (inset). Immunohistology, haematoxylin counterstain; bar = 20  $\mu\text{m}$ .



918 **Supplemental Figure 5**



919

920 Lung, K18-hACE2 mice. Composition of the inflammatory infiltrates. **A, B:** staining for  
921 macrophages (Iba1+). **A)** PBS-control animal. Macrophages are the dominant infiltrating cells  
922 in the consolidated areas and in the vasculitis. A – artery with infiltration of the wall. V – vein

923 with infiltration of the wall. B – bronchiole. Bar = 50  $\mu$ m. **B)** RBD-S-Dps animal, male.  
924 Macrophages are the dominant infiltrating cells in the focal infiltrates. A – artery. V – vein. B –  
925 bronchiole. Bar = 20  $\mu$ m. **C, D:** staining for T cells (CD3+). **C)** PBS-control animal. T cells are  
926 numerous in the consolidated areas and in the vasculitis. A – artery with infiltration of the wall  
927 and perivascular T cell accumulation. B – bronchiole. Bar = 50  $\mu$ m. **D)** RBD-S-Dps animal, male.  
928 T cells are numerous in the focal infiltrates. V – vein. Bar = 20  $\mu$ m. **E, F:** staining for CD4. **E)** PBS-  
929 control animal. Within the infiltrates, CD4 positive cells are numerous. V – vein. Bar = 20  $\mu$ m.  
930 **F)** RBD-S-Dps animal, male. Within the infiltrates, CD4 positive cells are present in moderate  
931 number. B – bronchiole. Bar = 20  $\mu$ m. **G, H:** staining for CD8. **G)** PBS-control animal. CD8  
932 positive cells are less numerous. V – vein. Bar = 20  $\mu$ m. **H)** RBD-S-Dps animal, male. CD8 positive  
933 cells are more abundant. V – vein. Bar = 20  $\mu$ m. Inset: CD8 positive cells are also present in the  
934 lumen of several alveoli. Bar = 10  $\mu$ m. **I, J:** staining for B cells (CD45R/B220+). **I)** PBS-control  
935 animal. B cells are observed in moderate numbers in the consolidated areas and are rare in the  
936 vasculitis. A – artery with infiltration of the wall. V – vein with infiltration of the wall. B –  
937 bronchiole. Bar = 50  $\mu$ m. **J)** RBD-S-Dps animal, male. B cells (CD45R/B220+) are observed in  
938 moderate numbers in the focal infiltrates. A – artery. B – bronchiole. Bar = 20  $\mu$ m. Inset: Focal  
939 peribronchial (B) B cell aggregate. Bar = 20  $\mu$ m. Immunohistology, haematoxylin counterstain.



940 **Supplemental Table 1**

941 Amino acid sequences of the proteins used in this work. Signal sequences for secretion in  
 942 mammalian cells are indicated in red.

Protein	Amino acid sequence
SpyC-Dps	MGHHHHHHGGSDSATHIKFSKRDEDEGKELAGATMELRDSSGKTIISTWISDGQVKDFYL YPGKYTFVETAAPDGYEVATAITFTVNEQGQVTVNGKATKGAHIGSEGSSGGQDKPK EEPKVVGVLEVLEKSGLDVKKLIEKLVKATAAEFTTYYYYTILRMHLTGMEGEGLEIA EDARLEDRLEHFELEMTQRIYELGGNLRDIRQLADLSACADAYLPENWKDPKEILKVLLE EAEQCAIRTWKEVCDMTYKDPRTYDLAQRILQEEIEHEAWFLELLYGRPSGHFRRSY PGEPPFSRKSRYE
SpyT2-NP (Nucleocapsid Protein)	MAHHHHHHGGSVPTIVMVDAYKRYKGGSGGSGGNTASWFTALTOHGKEDLKFPRGQGV PINTNSSPDDQIGYYRRATRIRGGDGKMKDLSRWYFYLLGTGPEAGLPYGANKDGI IWVATEGALNTPKDHIGTRNPANNAIVLQLPQGTTLPGKGYAEGSRGGSQASSRSSH RSRNSSRNSTPGSSRGTSPTARMAGNGGDAALALLLLDRLNQLESKMSGKGGQGGQTV TKKSAAEASKKPRQKRTATKAYNVTQAFGRRGPEQTQGNFGDQELIRQGTDYKHWPI AQFAPSASAFFGMSRIGMEVTPSGTWLTYTGAIKLDKDPNFKDQVILLNKHIDAYKTFP
RBD-SpyT2	( <b>MGILPSPGMPALLSLVSLLSVLLMGCVA</b> ) ETGITNLCPFGEVFNATRFASVYAWNRRKISNCVADYSVLYNSASFSTFKCYGVSPTK LNDLCFTNVYADSFVIRGDEVRQIAPGQTGKIADYNYKLPDDFTGCVIAWNSNNLDSK VGGNYNYLYRLFRKSNLKPFFERDISTEIQAGSTPCNGVEGFNCYFPLQSYGFQPTNG VGYQPYRVVLSFELLHAPATVCGPKKGTGGSGGSLNDIFEAQKIEWHEGGSHHHHH HHHGGSGGSGSVPTIVMVDAYKRYK
Spike	( <b>MGILPSPGMPALLSLVSLLSVLLMGCVA</b> ) ETGVNLTTRTQLPPAYTNSFTRGVYYPDKVFRSSVLHSTQDLFLPFFSNVTWFHAIHV SGTNGTKRFDNPVLPFNDGVYFASTEKSNIIRGWIFGTTLDSKTQSLLIIVNNATNVVI KVCFEQFCNDPFLGVYHKNKNSWMESEFRVYSSANNCTFEYVSQPFLLMDLEGKQGNF KNLREFVFKNIDGYFKIYSKHTPINLVRDLPOGFSALEPLVDLPIGINITRFQTLAL HRSYLTPGDSSSGWTAGAAAYVGYLQPRTFLLKYNENGTITDAVDCALDPLSETKCT LKSFTVEKGIYQTSNFRVQPTESIVRFPNITNLCPFGEVFNATRFASVYAWNRRKISN CVADYSVLYNSASFSTFKCYGVSPTKLNLCFTNVYADSFVIRGDEVRQIAPGQTGKI ADYNYKLPDDFTGCVIAWNSNNLDSKVGNYNYLYRLFRKSNLKPFFERDISTEIQAG STPCNGVEGFNCYFPLQSYGFQPTNGVGYQPYRVVLSFELLHAPATVCGPKKSTNLV KNKCVNFNFNGLTGTGVLTESNKKFLPFQQFGRDIADTTDAVRDPQLEILDITPCSF GGVSVITPGTNTSNQVAVLYQDVNCTEVPVAIHADQLTPTWRVYSTGNSVFQTRAGCL IGAHVNSYECDIPIGAGICASYQTQTNPSGASASSVASQSI IAYTMSLGAENSVAYS NNSIAIPTNFTISVTTTEILPVSMTKTSVDCTMYICGDSTECNLLLQYGSFCTQLNRA LTGIAVEQDKNTQEVFAQVKQIYKTPPIKDFGGFNFSQILPDPSPKSKRSFIEDLLFN KVTLADAGFIKQYGDCLGDI AARDLICAQKFNGLTVLPPLLTDEMAQYTSALLAGTI TSGWTFGAGAALQIPFAMQMAYRFNGIGVTQNVLYENQKLIANQFNSAIGKIQDSLSS TASALGKLQDVVNQNAQALNTLVKQLSSNFGAISSVLNDILSRLDPPAEVQIDRLIT GRLQSLQTYVTQQLIRAAEIRASANLAATKMSECVLGGQSKRVDFCGKGYHLMSFPQSA PHGVVFLHVTVYVPAQEKNFTTAPAI CHDGKAHFPREGVFSVNGTHWFVTRNFYEPQI ITTDNTFVSGNCDVVI GIVNNTVYDPLQPELDSFKEELDKYFKNHTSPDVLGDISGI NASVVNIQKEIDRLNEVAKNLNESLIDLQELGKYEQGGYIPEAPRDGQAYVRKDGW VLLSTFLGRSGSLEVLFGQPGGSGSLNDIFEAQKIEWHEGGSHHHHHH
Spike-SpyT2	( <b>MGILPSPGMPALLSLVSLLSVLLMGCVA</b> ) ETGVNLTTRTQLPPAYTNSFTRGVYYPDKVFRSSVLHSTQDLFLPFFSNVTWFHAIHV SGTNGTKRFDNPVLPFNDGVYFASTEKSNIIRGWIFGTTLDSKTQSLLIIVNNATNVVI KVCFEQFCNDPFLGVYHKNKNSWMESEFRVYSSANNCTFEYVSQPFLLMDLEGKQGNF

KNLREFVFKNIDGYFKIYSKHTPINLVRDLPOGFSALEPLVDLPIGINITRFQTLAL HRSYLTPGDSSSGWTAGAAAYYVGYLQPRTFLLKYNENGTITDAVDCALDPLSETKCT LKSFTVEKGIYQTSNFRVQPTESIVRFPNITNLCPFGEVFNATRFASVYAWNRKRISN CVADYSVLVNSASFSTFKCYGVSPTKLNDLCFTNVYADSFVIRGDEVQRQIAPGQTGKI ADYNYKLPDDFTGCVIAWNSNLDLSDKVGNYLYRLFRKSNLKPFFERDISTEIQAG STPCNGVEGFNCYFPLQSYGFQPTNGVGYQPYRVVLSFELLHAPATVCGPKKSTNLV KNKCVNFNFNGLTGTGVLTESNKKFLPFQFGRDIADTTDAVRDPQLEILDITPCSF GGVSVITPGTNTSNQVAVLYQDVNCTEVPVAIHADQLTPTWRVYSTGNSVFOFRAGCL IGAHEVNNSYECDIPIGAGICASYQTQTNSPGSASSVASQSI IAYTMSLGAENSVAYS NNSIAIPTNFTISVTTEILPVSMTKTSVDCTMYICGDSTECNLLLQYGSFCTQLNRA LTGIAVEQDKNTQEVFAQVKQIYKTPPIKDFGGFNFSQILPDPSKPSKRSFIEDLLFN KVTLADAGFIKQYGDCLGDI AARDLICAQKFNGLTVLPPLLTDemiaQYTSALLAGTI TSGWTFGAGAALQIPFAMQMAYRFNGIGVTQNVLYENQKLIANQFNSAIGKIQDSLSS TASALGKLQDVVNQNAQALNTLVKQLSSNFGAISSVLNDILSRLDPPEAEVQIDRLIT GRLQSLQTYVTQQLIRAAEIRASANLAATKMSECVLQSKRVDFCGKGYHLMSPQSA PHGVVFLHVTVVPAQEKNFTTAPAICHGDKAHFPREGVVFVSNGTHWFVTQRNFYEPQI ITTDNTFVSGNCDVVIGIVNNTVYDPLQPELDSFKEELDKYFKNHTSPDVDLGDISGI NASVVNIQKEIDRLNEVAKNLNESLIDLQELGKYEQGGSYIPEAPRDGQAYVRKDGW VLLSTFLGRSGTGGSGGSLNDIFEAQKIEWHEGGSHHHHHHHHGGSGGSGSVPTIV MVDAYKRYK
---

943